Three-Dimensional Impact: Energy-based Modeling of Tangential Compliance

Yan-Bin Jia
Department of Computer Science
Iowa State University
Ames, IA 50010, USA
jia@iastate.edu

Abstract

Impact is indispensable in robotic manipulation tasks in which objects and/or manipulators move at high speeds. Applied research using impact has been hindered by underdeveloped computational foundations for rigid body collision. This paper studies the computation of tangential impulse as two rigid bodies collide at a point with both tangential compliance and friction in the space. It extends Stronge's spring-based planar contact structure (Stronge 2000, pp. 95–96) to three dimensions by modeling the contact point as a massless particle able to move tangentially on one body while connected to an infinitesimal region on the other body via three orthogonal springs. Slip or stick is indicated by whether the particle is still or moving. Impact analysis is carried out using normal impulse rather than time as the only independent variable, unlike in previous work on tangential compliance. This is due to the ability of updating the energies stored on the three springs. Collision is governed by a system of differential equations solvable numerically. Modularity of the impact model makes it easy to be integrated into a multibody system, with one copy at each contact, in combination with a simultaneous impact model (Jia et al. 2011) that governs normal impulses at different contacts.

KEY WORDs—impact, tangential compliance, friction, tangential impulse, energy-based restitution, contact modes, sliding velocity

1 Introduction

Impact occurs over a very short time period when two or more bodies collide. During this period, a high force is applied and kinetic energy is restored, released (after a partial loss), or transferred to other bodies. We make use of impulsive forces to accomplish tasks that would otherwise be very difficult, if not impossible. Example actions include hammering a nail, cracking a boiled egg, pounding garlic with a mortar and pestle, beating a drum, hitting a tennis ball, smashing a volleyball, etc. On other occasions, we would like to reduce impulsive forces that might do harm to ourselves by extending their duration. Air bags in automobiles are designed for such purpose. So is much equipment in sports, for instance, baseball and boxing gloves, football helmets, gymnastic mats, etc.

Impact has applications in manufacturing operations and robotic tasks in which high-speed motions take place. A bowl feeder (Boothroyd and Redford 1968) vibrates parts to channel them

through a spiral inclined track. After going through collisions with some gates along the track, the parts will come out sorted in a small number of fixed orientations. Space robots need to minimize impulsive reaction forces from collisions with other free-floating objects (Yoshida and Nenchev 1995) or from landing on other planets, either inside spacecraft or by themselves.

Investigations on robot dynamics during impact have been centered around modeling of collisions between the robot and the environment (Zheng and Hemami 1985), design of impact control schemes for stable contact during such collisions (Volpe and Khosla 1993), and evaluation of the collision effects on the robot (Walker 1994). Though the first legged machine (Raibert 1986) appeared more than two decades ago, most walking robots today are still confined to labs performing statically stable gaits to avoid inertial effects. Addressing instability generated by fast walking and running (Garcia and de Santos 2005) clearly requires better understanding of the foot-ground collision. A large impulsive force can be generated by a humanoid robot without losing its balance by minimizing the angular momentum based on impact dynamics (Konno et al. 2011).

Short execution time gives the impulsive force an edge on efficiency over the static and dynamic forces. The usage of impulsive forces could potentially simplify the robotic mechanism needed to perform a manipulation task, while avoiding uncertainties accumulated over repeated complex operations. Despite this advantage and many potential applications, impulsive manipulation has remained an under-explored area in robotics with very little known work (Higuchi 1985; Izumi and Kitaka 1993; Partridge and Spong 1999; Hirai et al. 1999; Huang and Mason 2000; Han and Park 2001; Tagawa et al. 2010). This is primarily attributed to the fact that the foundation for rigid body impact is not fully developed, nor is any computational model surrounding it. Existing impact theories often seem either too simple to be realistic or too complex to be applicable in the presence of friction and tangential compliance. Discrepancies often exist between an introduced theory and the findings from an experiment intended for its validation.

Robotic manipulation frequently makes use of contact compliance and compliant motions. Implementable via force control of manipulators (Raibert and Craig 1981; Mason 1981; Khatib and Burdick 1986), compliant motions often reduce uncertainties while increasing dexterity and reliability in task executions. The classical peg-in-hole insertion (Whitney 1982), for instance, has been extensively studied in the robotics literature as a representative operation in assembly. Compliance also plays a critical role in improving robot safety (Sentis et al. 2010; Van Damme et al. 2010), which is the most important concern in human-robot interaction, an area that has seen growing interest with applications, such as robot assisted surgery and robot assistants for the elderly. Viewed in the path planning domain, compliant motions are on the surface of configuration space obstacles and may be planned over a graph of topological "contact states" (Tang and Xiao 2008).

Impact with tangential compliance has a large potential application in sports robotics. Skills in ball sports are essentially about how to strike balls to make them follow desired trajectories while moving and spinning fast enough to evade the opponents. Tangential compliance between a ball and a striker is often critical for imparting a desired ball motion. A table tennis player uses a loop drive with the racket grazing the ball to generate a large amount of topspin. This is a perfect example of impact with tangential compliance. In pocket billiards (Shamos 1993), compliance between the cue tip and the cue ball is essential for achieving desired post-shot speed and spinning of the cue ball. There are two objectives: to pocket an object ball, and to position the cue ball when it comes to stop so the next shot can continue comfortably.

In impact, compliance is attributed to restoration of kinetic energy, both normally and tangentially. Unfortunately, the role of tangential compliance had long been ignored with tangential

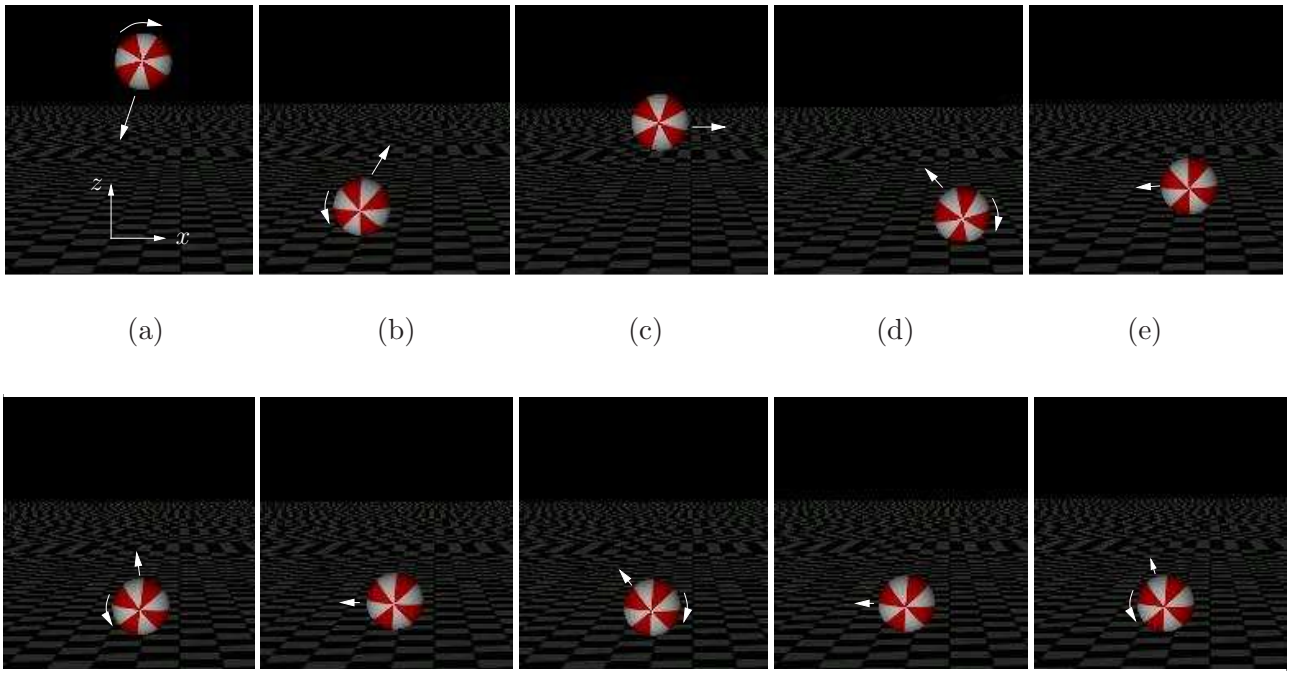

Figure 1: Five consecutive bounces of a ball.

dissipation of kinetic energy simply assumed for both contact modes — slip and stick — and attributed to Coulomb friction. Observation shows that a ball hitting the ground at a small incidence angle may bounce backward with a reversal of its rotation. Clearly, part of the tangential kinetic energy absorbed at contact can be restored after the impact, just like its normal counterpart.

Generally, during an impact between two bodies, the work done by the reaction force is converted into internal strain energy of which the elastic part can be recovered. Under compliance, not all the work done by the tangential force is lost to friction — part is returned just like the work done by the normal force component (treated in the classical impact theory). This could cause reversals of tangential motions after the impact — an effect that cannot be generated by friction. The effect of tangential compliance is an integral phenomenon of collision in reality, and is important for us to understand in the design of manipulation strategies.

This paper will develop a computational model for tangential compliance in three-dimensional impact that is based on evolution of the normal and tangential strain energies stored at contact. A companion submission (Jia et al. 2011) to the International Journal of Robotics Research describes a model for simultaneous impacts, and includes in the end its integration with the impact model for tangential compliance studied here to solve multibody impact problems. There the integrated model is demonstrated by simulating a massé billiard shot that matches the experimental data.

Figure 1 shows a scenario of the first five bounces initiated by a ball striking the plane at the origin (in (a)) with velocity $(-1, 0, -5)$ and angular velocity $(0, 2, 0)$. Because the ball's velocity and angular velocity are orthogonal, its center stays in the x-z plane during the bounces. The ball configurations immediately after the collisions are captured in (b), (d), (f), (h), and (j). In (c), (e),

(g), and (i), the ball rebounds to the highest positions between collisions with the table. Due to contact compliance, the first impact on the plane shown in (b) has reversed the ball's velocity in the x-direction and its angular velocity, both of which will be reversed again by the second impact in (d). The ball's kinetic energy decreases due to sliding friction that occurs during each impact. During each of the next three impacts depicted in (f), (h), and (j), contact compliance is not strong enough to reverse the ball's x-velocity, though it does reverse the direction of rotation. Coming out of the collision in (j), the ball's velocity has reduced to $(-0.088333, 0, 0.155565)$ and angular velocity to $(0, -0.279167, 0)$.

In the example, reversals of the ball's tangential and angular velocity are due to storage and (then partial) release of the ball's kinetic energy carried by its contact velocity. The phenomenon is similar to that of a particle bouncing back after hitting the free end of a horizontal spring with the other end fixed. Some of the ball's kinetic energy dissipates under sliding friction at contact during the collision. The example shows that tangential compliance and friction have different effects on impact.

1.1 Impact Dynamics and Contact Kinematics

This paper provides a computational study of the role of tangential compliance during an impact between two bodies $\mathcal{B}_1$ and $\mathcal{B}_2$ making point contact at p as shown in Figure 2. Let $\boldsymbol{F}$ be the contact force at p exerted by $\mathcal{B}_2$ on $\mathcal{B}_1$ during the impact. The integral of $\boldsymbol{F}$ over time during the impact is the impulse $\boldsymbol{I}$ exerted by $\mathcal{B}_2$. A reverse impulse $-\boldsymbol{I}$ is exerted on $\mathcal{B}_2$ by B_1 under Newton's third law. Since $\boldsymbol{F}$ goes to infinity as the impact period tends to zero, gravity is ignored. So the contact plane is drawn horizontal with $\mathcal{B}_1$ above $\mathcal{B}_2$.

The impulse $\boldsymbol{I}$ is decomposed into a component I_n along the contact normal $\hat{\boldsymbol{n}}$ at p and a tangential component $\boldsymbol{I}_\perp$. The normal component I_n accumulates throughout the impact. In solving the impact problem, I_n can be treated as the variable whose value will grow monotonically to a point decided by the applied impact law.

The tangential impulse $\boldsymbol{I}_\perp$, however, depends on a sequence of contact modes that occur during the impact. When the contact is sliding, the differential change $d\boldsymbol{I}_\perp$ is related to the differential accumulation dI_n under Coulomb's law of friction. It opposes the instantaneous slip direction. When the contact is sticking, $d\boldsymbol{I}_\perp$ is in a direction that counters the tendency of slip.[1]

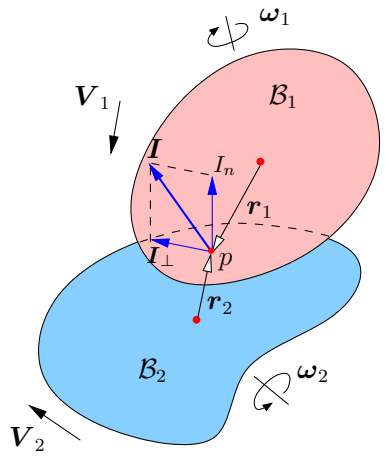

Figure 2: Impact between two bodies

Computation of the tangential impulse $\boldsymbol{I}_\perp$ and contact mode analysis during an impact are the focus of this paper. Contact mode is closely related to the tangential component of the relative velocity of the two bodies at p, which is governed by contact kinematics. As we will show, it is also related to the strain energy stored at contact during the impact.

We set up the world frame at p with its xy-plane coinciding with the tangent plane. As illustrated in Figure 2, for $i = 1, 2$, denote by $\boldsymbol{V}_i$ the velocity of the $\mathcal{B}_i$, and by $\boldsymbol{\omega}_i$ its angular velocity. For convenience, $\boldsymbol{\omega}_i$ is often described in terms of a fixed frame $\mathcal{F}_i$ instantaneously

[1]Sticking causes no energy dissipation in our model, introduced later.

coincident with the ith body's canonical frame at its center of mass. Under this canonical frame, the body's angular inertia matrix Q_i is diagonalized. Since the body does not move during the infinitesimal impact period, we can study the change in its angular velocity during the impact with respect to the same fixed frame $\mathcal{F}_i$. The orientation of $\mathcal{F}_i$ relative to the world frame is described by a rotation matrix R_i. In $\mathcal{F}_i$, let $\boldsymbol{r}_i$ be the vector from the center of mass of $\mathcal{B}_i$ to the contact point p. We have that

$$\begin{aligned} \boldsymbol{F} &= m_1\dot{\boldsymbol{V}}_1, \\ \boldsymbol{r}_1 \times (R_1^{-1}\boldsymbol{F}) &= Q_1\dot{\boldsymbol{\omega}}_1 + \dot{\boldsymbol{\omega}}_1 \times Q\dot{\boldsymbol{\omega}}_1, \end{aligned}$$

where the dot '.' denotes differentiation with respect to time. Integrate the above equations over a time period $[0, t]$, where $t \le \tau$, the impact duration:

$$\begin{aligned} \boldsymbol{I} &= m_1\Delta\boldsymbol{V}_1, \\ \boldsymbol{r}_1 \times (R_1^{-1}\boldsymbol{I}) &= Q_1\Delta\boldsymbol{\omega}_1. \end{aligned}$$

In the above, as $t \to 0$, the integral $\int_0^t \boldsymbol{\omega} \times Q_1\boldsymbol{\omega}\, dt \to 0$ since $\boldsymbol{\omega}$ is bounded.

We set up the impact equations for object $\mathcal{B}_1$ in a similar way. Solve for the changes in the velocities of two objects during the impact:

$$\begin{aligned} \Delta\boldsymbol{V}_1 &= \frac{1}{m_1}\boldsymbol{I} \qquad \text{and} \qquad \Delta\boldsymbol{\omega}_1 = Q_1^{-1}\Big(\boldsymbol{r}_1 \times (R_1^{-1}\boldsymbol{I})\Big), \\ \Delta\boldsymbol{V}_2 &= -\frac{1}{m_2}\boldsymbol{I} \qquad \text{and} \qquad \Delta\boldsymbol{\omega}_2 = -Q_2^{-1}\Big(\boldsymbol{r}_2 \times (R_2^{-1}\boldsymbol{I})\Big). \end{aligned} \tag{1}$$

Meanwhile, the contact velocity is of $\mathcal{B}_1$ relative to $\mathcal{B}_2$ at p:

$$\boldsymbol{v} = \boldsymbol{V}_1 + R_1(\boldsymbol{\omega}_1 \times \boldsymbol{r}_1) - \boldsymbol{V}_2 - R_2(\boldsymbol{\omega}_2 \times \boldsymbol{r}_2). \tag{2}$$

During the impact, it changes by the amount

$$\begin{aligned} \Delta\boldsymbol{v} &= \Delta\boldsymbol{V}_1 + R_1(\Delta\boldsymbol{\omega}_1 \times \boldsymbol{r}_1) - \Delta\boldsymbol{V}_2 - R_2(\Delta\boldsymbol{\omega}_2 \times \boldsymbol{r}_2) \\ &= \frac{1}{m_1}\boldsymbol{I} + R_1\left(\left(Q_1^{-1}\Big(\boldsymbol{r}_1 \times (R_1^{-1}\boldsymbol{I})\Big)\right) \times \boldsymbol{r}_1\right) - \frac{1}{m_2}(-\boldsymbol{I}) - R_2\left(\left(Q_2^{-1}\Big(\boldsymbol{r}_2 \times (R_2^{-1}(-\boldsymbol{I}))\Big)\right) \times \boldsymbol{r}_2\right) \\ &= \left(\frac{1}{m_1} + \frac{1}{m_2}\right)\boldsymbol{I} - \Big(R_1P_1Q_1^{-1}P_1R_1^{-1} + R_2P_2Q_2^{-1}P_2R_2^{-1}\Big)\boldsymbol{I} \\ &= \left(\frac{1}{m_1} + \frac{1}{m_2}\right)\boldsymbol{I} - S\boldsymbol{I}, \end{aligned} \tag{3}$$

where P_i, $i = 1, 2$, is the antisymmetric matrix such that $P_i\boldsymbol{u} = \boldsymbol{r}_i \times \boldsymbol{u}$ for any vector $\boldsymbol{u}$, and

$$S = R_1P_1Q_1^{-1}P_1R_1^{-1} + R_2P_2Q_2^{-1}P_2R_2^{-1}. \tag{4}$$

Thus, $\Delta\boldsymbol{v}$ is linear in the impulse with tangential component

$$\begin{aligned} \Delta\boldsymbol{v}_\perp &= (1 - \boldsymbol{n}\boldsymbol{n}^T)\Delta\boldsymbol{v} \\ &= \left(\frac{1}{m_1} + \frac{1}{m_2}\right)\boldsymbol{I}_\perp - (1 - \boldsymbol{n}\boldsymbol{n}^T)S\boldsymbol{I}. \end{aligned} \tag{5}$$

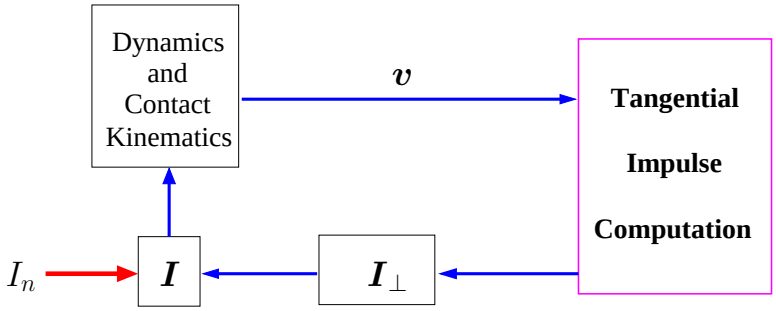

Figure 3: System of impact with tangential compliance.

In the above, we abuse the notation slightly to use the number 1 in $1 - \boldsymbol{n}\boldsymbol{n}^T$ for the 3×3 identity matrix, without introducing any ambiguity. The velocity $\boldsymbol{v}_\perp$ will be used in a contact mode analysis for computation of $\boldsymbol{I}_\perp$.

Figure 3 integrates impulse into the system dynamics. The entire system is modeled in the impulse space, not the time space. Computation of the tangential impulse $\boldsymbol{I}_\perp$ will rely on the use of several virtual contact springs to model strain energies stored and released at the contacts.

1.2 Paper Outline

Computation of tangential impulse is the key to solving an impact problem with friction and tangential compliance, even one as simple as Figure 1. For normal impulse, the use of an energetic coefficient of restitution (Stronge 1990) is the only existing law of restitution consistent with the law of energy conservation. For tangential impulse, an energy-based formulation is necessary to maintain such consistency. There is no reason to believe that the normal and tangential components of an impact would synchronize on compression and restitution. Even further, unlike the impact's normal component, its tangential component may switch between compression and restitution many times. In this paper, we will extend the structure of the linear model given by Stronge (2000, pp. 95–96) for planar impact with tangential compliance to develop a theory for 3-dimensional impact that is based on normal impulse only and consistent with both laws of Coulomb friction and energy conservation. Early development of the theory was described in Jia (2010).

Section 2 reviews the basic theory on single impact with frictionless contact, formulating the derivative of contact strain energy with respect to impulse, which will be used frequently in the subsequent development. Section 3 introduces a compliant impact model and describes the contact strain energies. Section 4 performs a detailed contact mode analysis. Section 5 summarizes a system of differential equations that governs the dynamics and contact kinematics with normal impulse as the only independent variable, and presents a numerical algorithm. The degenerate case of planar impacts is treated in Section 6. Section 7 shows that the post-impact velocities scale with the pre-impact velocities, which is an important property for any impact model to have. Two examples of a ball and a pencil striking a table, separately, are presented in Section 8 with plots of impulse and velocity curves and discussions over the effects of friction, tangential compliance, and the coefficient of restitution. Section 9 concludes with a summary and some future work.

1.3 Impact Overview

Under Newton's third law, all collisions conserve momentum. An elastic collision also conserves kinetic energy, while a plastic collision does not. Molecular collisions are elastic because there is no loss of energy. Collisions in our daily life (and virtually all in robotic tasks), however, are plastic. Solution of an impact problem requires determining the post-impact velocities from the impact configuration and pre-impact velocities. The problem is under-constrained by momentum conservation alone, so some extra law over impact needs to be imposed. Three commonly used ones, Newton's law, Poisson's hypothesis, and energy-based restitution, respectively specify the ratios between the speeds after and before the impact, between the impulse growths during two different impact phases (restitution and compression), and between the strain energies released and stored during these two phases.

1.3.1 Newton's Law

Newton's law of impact (Mason 2001, p. 212) asserts that the speed of an object after an impact is a constant fraction of that before the impact. The ratio, referred to as the *kinematic coefficient of restitution*, lies in the range $[0, 1]$. The law was applied very early on in the study of multiple impacts by Maclaurin (1742), and in particular in the study of elastic collision in a system of spheres by Bernoulli (1969). More recently, Ivanov (1995) examined four approaches to solving multiple impact problems with no friction based on Newton's law: independent restitutions at contacts, sequencing into successive impacts, a method of deformation, and a statistical method. The first two generate either unrealistic results or no unique solution. The third method is highly sensitive to initial conditions, while the fourth one has to consider all possible sequences of pairwise collisions (thus increasing the complexity significantly).

It is well known that Newton's law of impact could result in energy increase (Wang et al. 1992; Wang and Mason 1992). Also, for multiple impacts, it implies that still objects should remain still, which is clearly incorrect since energy often gets transferred to such objects. Consider a simple version of Newton's cradle (Brogliato 1999) where three balls are aligned horizontally with the leftmost ball having an initial velocity to start the collisions. All three balls may get velocities after the process (Liu et al. 2009). As another counterexample, when we drop a ping pong onto another one sitting on the table, the still ball will bounce up as well. Newton's law is generally inadequate for modeling multiple impacts and impacts with contact friction and tangential compliance.

1.3.2 Poisson's Hypothesis

Impact occurs in a very short time period with very high interaction force. Impulse, which integrates force over time and equals the change in momentum, is nevertheless finite. Therefore it is more convenient to conduct impact analysis in the impulse space rather than in the time space. Poisson's hypothesis (Routh 1905) states that an impact between two bodies begins with a compression phase until their approaching velocity decreases to zero, and follows with a restitution phase until the two bodies fully separate. The hypothesis also asserts that the impulse accumulated during restitution is a fraction, called the *kinetic coefficient of restitution*, of that accumulated during compression. His hypothesis, coupled with Coulomb's law of friction, has been widely applied in analysis of frictional impact. Such analysis requires correct detection of impact phases (compression and restitution) as well as contact modes (sliding and sticking).

Planar impact. When the sliding direction stays constant (with possible reversals), tangential impulse can be determined from normal impulse based on Coulomb's law via case-based reasoning. In the case of a planar impact, the total impulse stays in the same plane and grows along a polyline. Routh (1905) developed a graphical method that constructs the trajectory of impulse accumulation based on Poisson's hypothesis. It was applied in some subsequent studies of two-dimensional rigid-body collisions with friction. Wang and Mason (1992) classified impact and contact modes, deriving an analytical form of impulse for each case, and showed that Poisson's hypothesis should be used instead of Newton's law. Han and Gilmore (1989) considered impact with multiple contacts under a purely algebraic law. Ahmed et al. (1999) and Lankarani (2000) extended Routh's method to impact analysis for multibody mechanical systems with a similar classification that recognizes all modes of impact, providing expressions for normal and tangential impulses for all impact types.

Three-dimensional impact. To an impact in three dimensions, however, Routh's method hardly applies since the impulse grows along a space curve. The sliding direction generally varies during the impact. Darboux (1880) was the first to describe impact dynamics in terms of normal impulse in the form of a differential equation. Closed-form solution to the differential equation does not exist for many three-dimensional impact problems, which thus need to be solved via numerical integration. Darboux's result was later rediscovered by Keller (1986) who also used the governing differential equation to show that the direction of sliding varies during an impact. The work outlined a hypothesis-and-test method for contact mode checking and tangential impulse evaluation.

The above method of contact mode analysis was extended by Bhatt and Koechling (1994) who computed the flow pattern of the tangential velocity during an impact as well as the line of sticking, by setting up a differential equation of this velocity in terms of (scaled) normal impulse. The solution tangential velocity as a vector varies along a trajectory called a *flow*. It depends on inertial properties of bodies, the coefficient of friction, and the initial slip velocity. These flows are non-intersecting and together are referred to as the *hodograph* (Stronge 2000, pp. 74–78). Sliding contact is declared if the tangential relative velocity is non-zero, and sticking contact otherwise. When stick transits to slip, the slipping direction can be solved from the velocity equation. Applying the same contact mode analysis, Mirtich and Canny (1995) sequenced impacts among a collection of objects for storage in a priority queue and demonstrated impulse-based interactive simulation. Batlle (1996) studied how the geometry of the hodograph is affected by the coefficient of friction.

Linear complementarity methods Glocker and Pfeiffer (1995) introduced an impact model for two-dimensional contacts under Coulomb friction and Poisson's hypothesis that is based on a linear complementarity (LCP) formulation. Complementarity arises in the normal direction from non-negativeness of impulse and contact velocity when either compression or restitution ends, and in the tangential direction with a polyhedral approximation of the Coulomb friction cone. Assuming that the impacts at all contacts end compression and restitution simultaneously, the method finds impulses at the ends of compression and restitution via numerical integration of dynamics with two LCP formulations, one for each impact phase. The computation employs Lemke's algorithm (Cottle et al. 1996) for LCP problems that pivots like the simplex algorithm in linear programming. A similar formulation of multi-rigid-body impact problems with friction was carried out by Stewart and Trinkle (1996) with a time stepping (integration) scheme that extends

to a nonlinear complementarity (NCP) formulation. Proved to be energy dissipative, their method was modified by Anitescu and Portra (1997) in order to guarantee a solution (though multiple ones may exist). In graphics, Baraff (1993) employed Lemke's algorithm to compute impulsive forces as unbounded rays, though not always following Newton's law of dynamics. A survey of LCP-based methods for frictionless collision problem can be found in Glocker (2001).

The LCP formulation of impact has several drawbacks. It does not correspond to fundamental physical properties (Chatterjee and Ruina 1998). Lemke's algorithm only generates the impulse values after compression and restitution but does not describe how the impulse accumulates, which is important for contact mode analysis during the impact. Often the LCP solution is not unique, so ambiguities exist. The normal impulse may sometimes be too small to prevent penetration and has to be enlarged considerably without physical justification, yielding an unrealistic solution (Glocker and Pfeiffer 1995). Finally, over multiple impacts, the assumption that all impacts synchronize in compression and restitution is unrealistic.

Like Newton's impact law, Poisson's hypothesis may predict an increase in the kinetic energy (Wang et al. 1992; Stewart and Trinkle 1996). The hypothesis is applied to each of multiple impacts in an isolated way, whereas in simultaneous collisions compression and restitution of the impact at one contact also depends on those happening at other contacts. Analysis of impact based on the hypothesis has been a subject of controversy in order to be consistent with Coulomb's law of friction and the law of energy conservation.

Newton's impact law and Poisson's hypothesis yield the same solution to a direct impact, an impact with frictionless contact, or a frictional impact with sliding contact only (Wang and Mason 1992). They are also equivalent for multi-contact impacts, first treated by Moreau (1988), if all contacts are frictionless and have the same coefficient of restitution (Glocker 2001).

1.3.3 Energy-Based Restitution

The energy-based model developed by Stronge (1990) defines an *energetic coefficient of restitution* as the square root of the portion of the strain energy absorbed during compression to be released during restitution. This coefficient measures energy dissipation directly, and therefore is consistent with the law of energy conservation, unlike the other two impact laws. Under Stronge's energy-based hypothesis, Wang et al. (1992) integrated rigid body dynamics with contact stress models for simulation of processes with multiple frictional contacts. Other efforts applying energy-based restitution are on multiple frictionless impacts (Liu et al. 2008; Jia et al. 2008; Liu et al. 2009), and frictional impact with or without tangential compliance (Zhao et al. 2009; Jia 2010).

Stronge's hypothesis is the only one of the three aforementioned impact laws (on speed, impulse, and energy, respectively) that ensures non-negative energy loss from sources other than friction. The kinetic coefficient of friction under Poisson's hypothesis, for instance, is not consistent with energy conservation when the direction of frictional contact slip varies during collision. It is otherwise equivalent to the coefficient of energetic restitution for single impact unless the colliding bodies are rough and the impact configuration is eccentric (Stronge 2000, p. 28).

Energy-based restitution is effective at modeling simultaneous impacts where compression and restitution of the impact at one contact also depends on those happening at other contacts. Under Poisson's hypothesis, which applies to each impact in an isolated way, there may not be enough energy stored at the contact to provide the amount of impulse growth during restitution required by the hypothesis (Jia et al. 2008).

Liu et al. (2008) described a framework for frictionless multiple impacts in a multi-body system, where energetic coefficients of restitution were applied to individual impacts. Impulses were related to each other differentially, and numerical integration was always carried out over the impulse at the contact currently with the maximum potential energy. Their sequel paper (Liu et al. 2009) presented a numerical algorithm and included simulation results for several benchmark problems including Newton's cradle, the Bernoulli problem, etc. Around the same time, Jia et al. (2008) independently proposed a simultaneous impact model that observed the same differential relationship between impulses at various contacts. Their model formulated the physical process with a state transition diagram, where each state represented a different combination of contacts that were instantaneously active. Every collision instance yielded a sequence of states with proven termination/convergence. Aside from simulation, a ping pong experiment was presented to validate the state transition model.

1.4 Impact with Tangential Compliance

None of the frictional impact models mentioned in Section 1.3.2 under Poisson's hypothesis, including those applying LCP, handle tangential compliance. They assume that all the work done by the tangential reaction force is lost to friction and thus completely unrecoverable. However, in many collisions, tangential compliance is not negligible and sometimes plays a prominent role. Under compliance, part of the tangential work is converted into elastic internal energy to be released later, while the remaining part dissipates under friction.

We cannot always exclude tangential impulse from the velocity equations due to its non-negligible effect on the impact outcome. Newton's impact law was augmented with an empirical formula for tangential impulse in terms of normal impulse and the approaching and separating velocities (Smith1991), or with a tangential coefficient of restitution that specifies the ratio between tangential and normal contact velocities before and after an impact (Bilbao et al. 1989; Brach1989). These approaches did not exactly follow Coulomb's law of friction. Johansson (2001) used a time stepping method for numerical integration that discretized dynamic and kinematic equations with Coulomb friction constraints. This method unrealistically assumed equal tangential and normal coefficients of restitution at all contacts, and presented no contact mode analysis.

Mindlin (1949) studied two spheres pressed together under a normal force while subjected to a tangential force, obtaining a condition for slip consistent with Coulomb's friction law. He found that stick would occur over a central circular region with microslips in a surrounding ring-shaped region. Applying the Hertz contact theory, Maw et al. (1976) investigated tangential compliance during the impact of an elastic sphere on a half-space, by dividing the contact area into a set of concentric annuli as sticking and slipping regions with the application of the elasticity theory.

Stronge (1994; 2000) developed a lumped parameter representation[2] of tangential compliance, and applied a time-dependent analysis to track the changes in the tangential velocity during a collision. His model could predict slip or stick at the contact under Coulomb's law. However, without knowing the duration of impact, the analysis could only be used to perceive contact modes qualitatively rather than to carry out specific computation. Stronge (2000) claimed that the frictional energy loss depended on the sliding speed[3], correcting his earlier statement (Stronge 1994) that it depended on the tangential relative velocity[4]. But it was not until the recent work by Hien (2010) that the formulation of frictional dissipation was completed. In our paper, such dissipation will be

[2]Such representation was earlier used by Mills and Nguyen (1992) over normal compliance.

[3]of a fictional massless particle attached to one body via virtual springs while moving on the other body

[4]obtained from contact kinematics

accounted for, as the tangential component of the contact strain energy is stored and released by two tangential springs.

In their study of planar frictional impacts, particularly the problem of a dimer bouncing on a vibrated plate, Zhao et al. (2009) used energetic coefficients of friction to model the normal impulses at various contacts that are related to each other differentially. When a contact sticks, a "correlation coefficient of friction" was used to relate the derivatives of the tangential impulse to the normal impulse. This coefficient depends on the geometry and masses of the two objects in contact but is irrelevant to the work done by the tangential force that could be partially released due to compliance. Thus an inconsistency arises in the treatments of normal and tangential impulses. Also, there is no reason that the differential ratio between the tangential and normal impulses must be a constant.

2 Single Impact with Frictionless Contact

In this section, we give a very brief review of single impact with frictionless contact. Consider the classical problem of a particle of mass m with downward velocity $v_0 < 0$ striking a horizontal table. The contact force F is non-negative in the duration τ of the impact, with $F = 0$ attained only at the beginning and end of the interaction. Since the force is physically continuous, it is integrable over $[0, t]$, $0 \le t \le \tau$, generating the impulse $I = \int_0^t F\,dt$. Conversely, the impulse is differentiable during the impact with $\dot{I} = F$. Since $F > 0$ in the middle of the physical process, we infer that there exists a one-to-one correspondence between t and I.

During the impact, gravity of the particle can be ignored since it is significantly less than the impulsive force F. Newton's second law states that $F = m\dot{v}$, where v is the particle's velocity. Integration of the equivalent equation $m\dot{v} = \dot{I}$ yields the ball velocity during the impact:

$$v = v_0 + \frac{I}{m}. \tag{6}$$

Namely, the total impulse is equal to the particle's change in momentum. Since the rebound velocity of the particle is no more than $-v_0$, the total impulse is finite. Ideally, the impact happens in infinitesimal time. As $\tau \to 0$, $F \to \infty$ in order to keep the integral I finite.

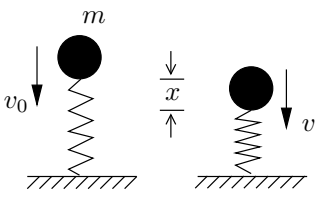

Figure 4: Particle impacting a table.

The impact is best analyzed in the impulse space. For better modeling, we attach a virtual spring with stiffness k at the contact point between the particle and the table, as shown in Figure 4. Let x measure the change in the virtual spring's length from its rest length, so its value is negative when the spring is compressed. We obtain the contact force $F = -kx$, and the potential energy $E = \frac{1}{2}kx^2$, which is zero only when the impact begins and finishes. Meanwhile, the ball's velocity is

$$v = \dot{x}. \tag{7}$$

The impact can be divided into two stages (Mason 2001, p. 212): compression and restitution. During compression, the particle's kinetic energy is transformed into the potential energy E of the spring. When compression ends, the energy reaches its maximum value $E_{\max}$. At this moment, the particle's velocity becomes zero, which by (6) gives the impulse $I = -mv_0$ exerted up to this point. During restitution, the elastic portion of the stored energy, of the amount $e^2 E_{\max}$, is released. Here

e, $0 \le e \le 1$, is referred to as the *energetic coefficient of restitution*.[5] The remaining portion $(1-e^2)E_{\max}$ is simply dissipated due to some irreversible internal deformation. The energy release keeps the impulse growing by an additional amount of $-emv_0$, ending the impact with the particle velocity $-ev_0$.

We adopt the explanation by Stronge (2000, p. 1998) for the energy loss[6]: When compression ends the spring stiffness suddenly increases by a factor of $1/e^2$. Such increase may be attributed to the hardening of the material due to some irreversible deformation.[7] Then, continuity of F implies that simultaneously the change in length of the spring reduces to a fraction e^2 of its previous value.

We obtain the time derivative of impulse in terms of energy:

$$\begin{aligned} \dot{I} &= F = -kx \\ &= \sqrt{2kE}. \end{aligned} \tag{8}$$

The derivative is well-defined at the impact phase transition where F is continuous. Under equation (8), differentiation with respect to time can be converted to differentiation with respect to impulse merely via division of $\sqrt{2kE}$.

Given the one-to-one correspondence between I and t, E can be described as a function of I, despite that the loss of energy after compression is directly due to deformation, not I. The function E has zero values at the start and the end of the impact, and the only discontinuity at the end of compression. It is differentiable during each impact phase:

$$\begin{aligned} \frac{dE}{dI} &= \frac{\dot{E}}{\dot{I}} = \frac{d(\frac{1}{2}kx^2)/dt}{-kx} = -\dot{x} \\ &= -v \qquad \text{by (7)} \qquad (9) \\ &= -\left(v_0 + \frac{I}{m}\right), \qquad \text{by (6).} \qquad (10) \end{aligned}$$

The third equation above holds because the stiffness k does not change its value during compression or restitution. Since I is continuous, at the impact phase switch the left and right derivatives of E, also given by (10), are equal.

Integration of equation (10) yields a quadratic relationship between E and I. The strain energy reaches its maximum $\frac{1}{2}mv_0^2$ when compression ends at $\dot{x} = 0$, that is, when $I = -mv_0$. Restitution begins after a loss of a fraction $1 - e^2$ of the maximum energy. The energy-impulse relation during the impact is given as

$$E = \begin{cases} -v_0 I - \frac{I^2}{2m}, & \text{if } I \le -mv_0; \\ -v_0 I - \frac{I^2}{2m} + \frac{1}{2}(e^2-1)mv_0^2, & \text{if } I > -mv_0. \end{cases} \tag{11}$$

[5]When friction exists at the contact and the direction of contact slip varies during a collision, Poisson's kinetic coefficient of restitution is not consistent with energy conservation (Stronge 2000, p. 47). It is otherwise equivalent to e for single impact unless the bodies in impact are rough and the impact configuration is eccentric (Stronge 2000, p. 28).

[6]An alternative, used by both Liu et al. (2008) and Jia et al. (2008), is not to change the stiffness at the impact phase switch but rather ends restitution when the energy reduces to $E = (1-e^2)E_{\max}$. Nevertheless, this approach seems to model the physical process less accurately and could introduce complications if compression switches back to restitution in simultaneous collisions, a phenomenon also remarked in Liu et al. (2008).

[7]Here we assume in reality that material deformation happens in a much shorter time period than impact.

Figure 5 plots E parametrized with I over $[0, -mv_0(1+e)]$. The curve consists of two halves of the same parabola above the I-axis, with the right half translated downward by $\frac{1}{2}(1-e^2)mv_0^2$, the amount of energy loss. The energy derivative with respect to the impulse exists as (10) if $I \neq -mv_0$. The curve is discontinuous at $I = -mv_0$.

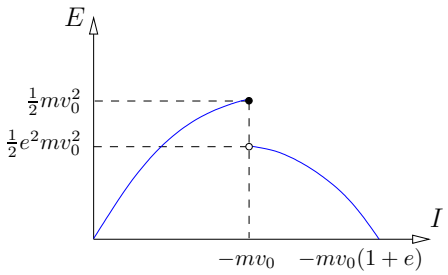

Figure 5: Energy evolution during impact.

3 Tangential Impulse

Since gravitational forces are negligible compared to the very large impulsive force at their contact, we re-orient the system configuration (cf. Figure 2) to keep the contact tangent plane horizontal. At the point of contact we set up a frame defined by the unit normal vector $\hat{\boldsymbol{n}}$ and two orthogonal tangent vectors $\hat{\boldsymbol{u}}$ and $\hat{\boldsymbol{w}}$ such that $\hat{\boldsymbol{u}} \times \hat{\boldsymbol{w}} = \hat{\boldsymbol{n}}$.

The direction $\hat{\boldsymbol{u}}$ is chosen as follows. If the tangential component $\boldsymbol{v}_{0\perp}$ of the initial contact velocity $\boldsymbol{v}_0$ is non-zero, that is, if $\boldsymbol{v}_0 \times \hat{\boldsymbol{n}} \neq 0$, $\hat{\boldsymbol{u}}$ opposes the direction of $\boldsymbol{v}_{0\perp}$. Otherwise, it opposes the tangential component of $S\hat{\boldsymbol{n}}$, where S is given in (4), if $\hat{\boldsymbol{n}}$ is not an eigenvector of S. If $\boldsymbol{v}_0 \times \hat{\boldsymbol{n}} = 0$ and $\hat{\boldsymbol{n}}$ is an eigenvector of S, $\hat{\boldsymbol{u}}$ is arbitrarily chosen in the tangent plane. More formally, we have

$$\hat{\boldsymbol{u}} = \begin{cases} \dfrac{\boldsymbol{v}_{0\perp}}{\|\boldsymbol{v}_{0\perp}\|}, & \text{if } \boldsymbol{v}_0 \times \hat{\boldsymbol{n}} \neq 0; \\ -\dfrac{(1-\hat{\boldsymbol{n}}\hat{\boldsymbol{n}}^T)S\hat{\boldsymbol{n}}}{\|(1-\hat{\boldsymbol{n}}\hat{\boldsymbol{n}}^T)S\hat{\boldsymbol{n}}\|}, & \text{if } \boldsymbol{v}_0 \times \hat{\boldsymbol{n}} = 0 \text{ but } \hat{\boldsymbol{n}} \text{ is not an eigenvector of } S; \\ \text{any unit vector orthogonal to } \hat{\boldsymbol{n}}, & \text{otherwise.} \end{cases} \tag{12}$$

As we will see in Section 6, if the impact degenerates into a planar one, the above choice of $\hat{\boldsymbol{u}}$ defines a plane with $\hat{\boldsymbol{n}}$ in which the impulse grows.

Note that $v_{0n} = \boldsymbol{v}_0 \cdot \hat{\boldsymbol{n}} < 0$ must hold for the collision to happen. This condition is assumed true in the rest of the paper.

All vectors will be projected along the three directions $\hat{\boldsymbol{u}}, \hat{\boldsymbol{w}}$, and $\hat{\boldsymbol{n}}$. In particular, the contact force $\boldsymbol{F}$ exerted on the upper body, the impulse $\boldsymbol{I}$, as well as the contact velocity $\boldsymbol{v}$ are decomposed:

$$\begin{aligned} \boldsymbol{F} &= F_u\hat{\boldsymbol{u}} + F_w\hat{\boldsymbol{w}} + F_n\hat{\boldsymbol{n}}, \\ \boldsymbol{I} &= I_u\hat{\boldsymbol{u}} + I_w\hat{\boldsymbol{w}} + I_n\hat{\boldsymbol{n}}, \\ \boldsymbol{v} &= v_u\hat{\boldsymbol{u}} + v_w\hat{\boldsymbol{w}} + v_n\hat{\boldsymbol{n}}. \end{aligned} \tag{13}$$

The initial contact velocity $\boldsymbol{v}_0 = v_{0u}\hat{\boldsymbol{u}} + v_{0w}\hat{\boldsymbol{w}} + v_{0n}\hat{\boldsymbol{n}}$ has no component along $\hat{\boldsymbol{w}}$, i.e., $v_{0w} = 0$, given the definition of $\hat{\boldsymbol{u}}$ in (12).

3.1 Virtual Contact Springs

To model tangential compliance, we first extend the planar contact structure used by Stronge (2000, pp. 95–96) to three dimensions. As shown in Figure 6, the infinitesimal contact area on the upper body does not directly touch the lower body. It is instead connected to a massless particle p via three springs that are respectively aligned with $\hat{\boldsymbol{n}}$, $\hat{\boldsymbol{u}}$, and $\hat{\boldsymbol{w}}$. The particle moves in the contact tangent plane during the impact. The three springs are respectively referred to as the n-, u-, and w-springs.

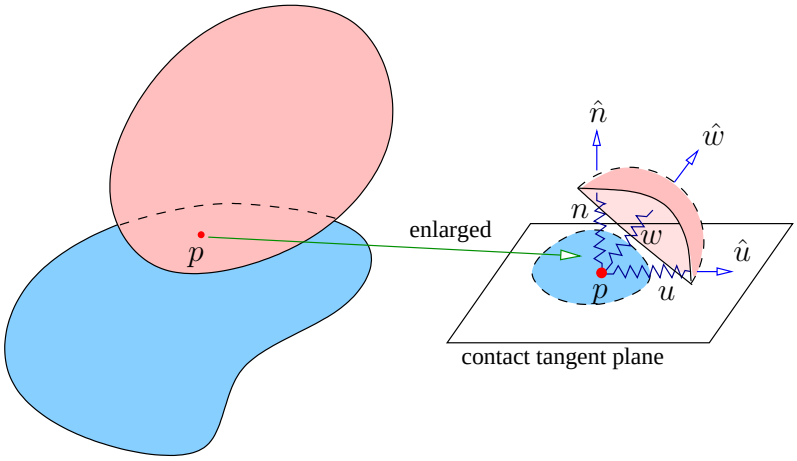

Figure 6: Contact structure.

The tangential u-spring and w-spring have the same stiffness $k_\perp$ which remains constant throughout the impact. The normal spring has original stiffness k_0 which will increase to k_0/e^2 at the end of compression according to Stronge's explanation of energy loss as described in Section 2. The ratio $\eta_0^2 = k_0/k_\perp$ is often considered a constant which depends on Young's moduli and Poisson's ratios of the materials in contact.[8] In the analysis, we will be using the ratio

$$\eta^2 = k/k_\perp, \tag{14}$$

where $\eta = \eta_0$ during compression and $\eta = \eta_0/e$ during restitution.

With a slight abuse of notation, we denote by n, u, w the *changes in length* of the n-, u-, and w- springs connected to the particle p, and E_n, E_u, E_w the strain energies these springs store, respectively. The contact force components and the strain energies are given below:

$$F_n = -kn \geq 0, \quad F_u = -k_\perp u, \quad F_w = -k_\perp w; \tag{15}$$

$$E_n = \frac{1}{2}kn^2, \qquad E_u = \frac{1}{2}k_\perp u^2, \quad E_w = \frac{1}{2}k_\perp w^2. \tag{16}$$

3.2 Impulse Derivatives

Our idea is to describe the impact in terms of the normal impulse I_n. Let a prime '′' always refer to differentiation with respect to I_n which has a one-to-one correspondence with time.

Combining the first equations from (15) and (16), the change rate of the normal impulse I_n over time can be described in terms of the strain energy E_n:

$$\dot{I}_n = \frac{dI_n}{dt} = F_n = \sqrt{2kE_n}. \tag{17}$$

The derivative is well-defined at the impact phase transition where F_n stays continuous despite sudden change in stiffness from k_n to k_n/e_n^2. Since $\dot{n} = v_n$, I_n and E_n assume the same relationship

[8] For normal indentation by a rigid circular punch on an elastic half space, Johnson (1985, pp. 361–366) showed that $\eta_0^2 = \frac{2-\nu}{2(1-\nu)}$, where ν is Poisson's ratio of the half space. For most materials, Poisson's ratio values ranges between 0 and 0.5.

as in the case of a single impact described in Section 2 with (9) replaced by

$$E_n' = \frac{dE_n}{dI_n} = \frac{\dot{E}_n}{\dot{I}_n} = \frac{kn\dot{n}}{-kn} = -\dot{n} = -v_n. \tag{18}$$

Since v_n depends on the two object's velocities, we cannot integrate the equation directly to get a closed form for E_n like the one given in (11).

Similar to (17), we obtain the change rates of the two tangential impulses in terms of the strain energies stored in the u- and w-springs:

$$\dot{I}_u = F_u = -\alpha\sqrt{2k_\perp E_u}, \tag{19}$$

$$\dot{I}_w = F_w = -\beta\sqrt{2k_\perp E_w}, \tag{20}$$

where α and β are the sign variables that respectively tell whether the two springs are being extended or compressed, namely,

$$\alpha = \begin{cases} 1 & \text{if } u \geq 0, \\ -1 & \text{if } u < 0; \end{cases} \qquad \text{and} \qquad \beta = \begin{cases} 1 & \text{if } w \geq 0, \\ -1 & \text{if } w < 0. \end{cases} \tag{21}$$

The three equations in (16) yield

$$n = -\sqrt{\frac{2E_n}{k}}, \qquad u = \alpha\sqrt{\frac{2E_u}{k_\perp}}, \qquad \text{and} \qquad w = \beta\sqrt{\frac{2E_w}{k_\perp}}. \tag{22}$$

Note that $n \leq 0$ throughout the impact.

Equation (17) is important because it allows us to convert any derivative with respect to time into one with respect to the normal impulse I_n simply by a division over $\sqrt{2kE_n}$. Thus, computation can proceed without the time variable. To illustrate, we write the derivatives of the two tangential impulses with respect to I_n as follows:

$$I_u' = \frac{\dot{I}_u}{\dot{I}_n} = -\alpha\sqrt{\frac{2k_\perp E_u}{2kE_n}} = -\frac{\alpha}{\eta}\sqrt{\frac{E_u}{E_n}}. \tag{23}$$

$$I_w' = -\frac{\beta}{\eta}\sqrt{\frac{E_w}{E_n}}. \tag{24}$$

As we will see later, the normal and tangential stiffnesses will always appear together as a ratio.

As I_n accumulates, I_u and I_w vary according to (23) and (24). The impulse $\boldsymbol{I} = I_u\hat{\boldsymbol{u}} + I_w\hat{\boldsymbol{w}} + I_n\hat{\boldsymbol{n}}$ varies along a curved trajectory parametrized by I_n. This trajectory is referred to as the *impulse curve*.

3.3 Compressions and Extensions of Tangential Springs

To evaluate the derivatives (23) and (24) of the tangential impulses, we need to keep track of whether each tangential spring is being compressed (e.g., $u < 0$) or elongated (e.g., $u > 0$), in order to determine the values of the sign variables α and β defined in (21).

The changes in length of the two springs are

$$u = \int_0^t \dot{u}\, dt = \int_0^{I_n} \frac{\dot{u}}{\sqrt{2kE_n}}\, dI_n, \tag{25}$$

$$w = \int_0^{I_n} \frac{\dot{w}}{\sqrt{2kE_n}}\, dI_n. \tag{26}$$

We cannot determine u and w unless k is known. However, because all we need are their signs to evaluate α and β, it suffices if their values after some scaling can be tracked.

Suppose that compression ends with the normal impulse value $I_n = I_c$ and restitution ends with $I_n = I_r$. We introduce two integrals:

$$G_u = \begin{cases} \int_0^{I_n} \frac{\dot{u}}{\sqrt{E_n}}\, dI_n, & \text{if } I_n \in [0, I_c), \\ \int_0^{I_c} \frac{\dot{u}}{\sqrt{E_n}}\, dI_n + \int_{I_c}^{I_n} e \frac{\dot{u}}{\sqrt{E_n}}\, dI_n, & \text{if } I_n \in [I_c, I_r]; \end{cases} \tag{27}$$

$$G_w = \begin{cases} \int_0^{I_n} \frac{\dot{w}}{\sqrt{E_n}}\, dI_n & \text{if } I_n \in [0, I_c), \\ \int_0^{I_c} \frac{\dot{w}}{\sqrt{E_n}}\, dI_n + \int_{I_c}^{I_n} e \frac{\dot{w}}{\sqrt{E_n}}\, dI_n, & \text{if } I_n \in [I_c, I_r]; \end{cases} \tag{28}$$

Each of G_u and G_w is a sum of subintegrals computed over a sequence of contact modes during the impact. The increments of G_u and G_w within a contact mode are computed by integrating $\dot{u}/\sqrt{E_n}$ and $\dot{w}/\sqrt{E_n}$, respectively, over $[I_n^{(0)}, I_n]$, where $I_n^{(0)}$ is the value of the normal impulse when the contact mode started. If compression ends during the contact mode, the integrands need to be scaled by the coefficient of restitution e for the values of I_n during restitution.

Comparing (27) and (28) respectively with (25) and (26) and noting that $k = k_0$ during compression and $k = k_0/e^2$ during restitution, we have

$$G_u = \sqrt{2k_0}u \quad \text{and} \quad G_w = \sqrt{2k_0}w. \tag{29}$$

Now, we need only keep track of G_u and G_w for the signs of u and w.

The second usage of G_u and G_w is for updating the tangential strain energies as follows:

$$E_u = \frac{1}{2}k_\perp u^2 = \frac{G_u^2}{4\eta_0^2}, \tag{30}$$

$$E_w = \frac{G_w^2}{4\eta_0^2}. \tag{31}$$

The change rates $\dot{u}$ and $\dot{w}$ in the lengths of the u- and w-springs turn out to be independent of the stiffness k of the normal spring, as we will derive below for both contact modes: stick and slip.

4 Contact Mode Analysis

The contact structure in Figure 6 provides a convenient way of analyzing contact modes during the impact in terms of the strain energies stored in the springs, and obtaining the change rates $\dot{u}$ and $\dot{w}$ of the lengths of the tangential springs (which are in turn used for updating the strain energies).

4.1 Sliding Velocity

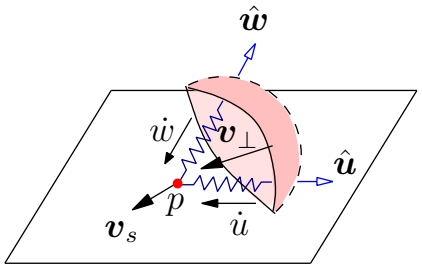

Figure 7: Sliding velocity of contact particle.

The contact velocity is $\boldsymbol{v} = \boldsymbol{v}_0 + \Delta\boldsymbol{v}$, where $\boldsymbol{v}_0$ is the initial contact velocity and $\Delta\boldsymbol{v}$ is given in (3). Denote its tangential component at the contact as $\boldsymbol{v}_\perp$. Then the particle p is moving in the contact tangent plane at velocity

$$\boldsymbol{v}_s = \boldsymbol{v}_\perp - \dot{u}\hat{\boldsymbol{u}} - \dot{w}\hat{\boldsymbol{w}}. \tag{32}$$

See Figure 7. When $\boldsymbol{v}_s = 0$, i.e., $\boldsymbol{v}_\perp = \dot{u}\hat{\boldsymbol{u}} + \dot{w}\hat{\boldsymbol{w}}$, the contact sticks. In this case, the relative motion of the upper body to the lower body in the contact plane is completely absorbed by the two tangential springs so that the particle exhibits no motion. When $\boldsymbol{v}_s \neq 0$, the contact is sliding with velocity $\boldsymbol{v}_s$, which is accordingly referred to as the *sliding velocity*.

In the case of slip, under Coulomb's law, the tangential contact force $\boldsymbol{F}_\perp = -\mu F_n \hat{\boldsymbol{v}}_s$, where $\hat{\boldsymbol{v}}_s = \boldsymbol{v}/\|\boldsymbol{v}\|$ is the sliding direction. Meanwhile, the force exerts on the upper body via the u- and w-springs: $\boldsymbol{F}_\perp = -k_\perp(u\hat{\boldsymbol{u}} + w\hat{\boldsymbol{w}})$. Equate the two forms of $\boldsymbol{F}_\perp$:

$$k_\perp(u\hat{\boldsymbol{u}} + w\hat{\boldsymbol{w}}) = \mu F_n \hat{\boldsymbol{v}}_s. \tag{33}$$

Switch the two sides of (32), and substitute (33) for $\hat{\boldsymbol{v}}_s$ in:

$$\boldsymbol{v}_\perp - \dot{u}\hat{\boldsymbol{u}} - \dot{w}\hat{\boldsymbol{w}} = \|\boldsymbol{v}_s\|\hat{\boldsymbol{v}}_s = \frac{k_\perp}{\mu F_n}\|\boldsymbol{v}_s\|(u\hat{\boldsymbol{u}} + w\hat{\boldsymbol{w}}). \tag{34}$$

Equation (34) also holds for the sticking contact where it reduces to $\boldsymbol{v}_\perp = \dot{u}\hat{\boldsymbol{u}} + \dot{w}\hat{\boldsymbol{w}}$ since $\boldsymbol{v}_s = 0$. Take dot products of $\hat{\boldsymbol{u}}$ and $\hat{\boldsymbol{w}}$ separately with both sides of (34):

$$\begin{aligned} \boldsymbol{v}_\perp \cdot \hat{\boldsymbol{u}} - \dot{u} &= \frac{k_\perp}{\mu F_n}\|\boldsymbol{v}_s\|u, \\ \boldsymbol{v}_\perp \cdot \hat{\boldsymbol{w}} - \dot{w} &= \frac{k_\perp}{\mu F_n}\|\boldsymbol{v}_s\|w. \end{aligned}$$

To eliminate the right hand sides above, we first multiply both equations with w and u, respectively, and then subtract one from another. This yields

$$\begin{aligned} w\dot{u} - u\dot{w} &= (\boldsymbol{v}_\perp \cdot \hat{\boldsymbol{u}})w - (\boldsymbol{v}_\perp \cdot \hat{\boldsymbol{w}})u \\ &= (\boldsymbol{v} \cdot \hat{\boldsymbol{u}})w - (\boldsymbol{v} \cdot \hat{\boldsymbol{w}})u \\ &= v_u w - v_w u. \end{aligned} \tag{35}$$

The above equation also holds for both contact modes just like (34) does.

4.2 Energy Dissipation

During the impact, the total energy (kinetic and strain) dissipates due to irreversible internal deformation in the normal direction and contact friction in the tangential direction. The first type of dissipation is characterized by the energetic coefficient of restitution e with a loss of $1 - e^2$ times the energy component carried by the initial normal contact velocity.

The second type of dissipation happens to the energy component due to the initial tangential contact velocity. Let $E_\perp \geq 0$ be the amount of energy dissipated during slip. We have

$$\begin{aligned} \dot{E}_\perp &= -\boldsymbol{F}_\perp \cdot \boldsymbol{v}_s \\ &= \mu \dot{I}_n \|\boldsymbol{v}_s\| \qquad\qquad \text{since } \boldsymbol{F}_\perp = -\mu F_n \hat{\boldsymbol{v}}_s \text{ when } \boldsymbol{v}_s \neq 0 \\ &= \mu \dot{I}_n \|\boldsymbol{v}_\perp - \dot{u}\hat{\boldsymbol{u}} - \dot{w}\hat{\boldsymbol{w}}\|. \end{aligned}$$

The rate of dissipation with respect to the normal impulse is

$$E'_\perp = \mu \cdot \|\boldsymbol{v}_\perp - \dot{u}\hat{\boldsymbol{u}} - \dot{w}\hat{\boldsymbol{w}}\|. \tag{36}$$

When the contact sticks, $\boldsymbol{v}_s = 0$ and hence $E'_\perp = 0$. Kinetic energy gets converted into strain energy or vice versa with no loss. When the contact slips, $E'_\perp > 0$ since the sliding velocity opposes $\boldsymbol{F}_\perp$. In Sections 4.3 and 4.4, we will derive closed forms for $\dot{u}$ and $\dot{w}$ and see that they depend on the contact velocity $\boldsymbol{v}$ and the strain energies E_u, E_w, E_n stored by the three virtual springs.

4.3 Stick

When the contact sticks, $\boldsymbol{v}_s = 0$, which by (32) implies

$$\boldsymbol{v}_\perp = \dot{u}\hat{\boldsymbol{u}} + \dot{w}\hat{\boldsymbol{w}}. \tag{37}$$

Take dot products of the above equation with $\hat{\boldsymbol{u}}$ and $\hat{\boldsymbol{w}}$, respectively:

$$\dot{u} = \boldsymbol{v}_\perp \cdot \hat{\boldsymbol{u}} = v_u, \tag{38}$$

$$\dot{w} = v_w. \tag{39}$$

Now, let us take a look at the motion of the upper body $\mathcal{B}_1$ relative to the lower body $\mathcal{B}_2$ in the contact tangent plane when the contact sticks. Differentiate (37):

$$\frac{d}{dt}(\boldsymbol{v}_\perp) = \frac{d}{dt}(\Delta \boldsymbol{v}_\perp) = \ddot{u}\hat{\boldsymbol{u}} + \ddot{w}\hat{\boldsymbol{w}}. \tag{40}$$

Under (5) and with the use of (16), the left hand side of the above equation is

$$\begin{aligned} \frac{d}{dt}(\Delta \boldsymbol{v}_\perp) &= \left(\frac{1}{m_1} + \frac{1}{m_2}\right) \dot{\boldsymbol{I}}_\perp - (1 - \boldsymbol{n}\boldsymbol{n}^T) S \dot{\boldsymbol{I}} \\ &= \left(\frac{1}{m_1} + \frac{1}{m_2}\right) (F_u \hat{\boldsymbol{u}} + F_w \hat{\boldsymbol{w}}) - (1 - \boldsymbol{n}\boldsymbol{n}^T) S (F_u \hat{\boldsymbol{u}} + F_w \hat{\boldsymbol{w}} + F_n \hat{\boldsymbol{n}}) \\ &= -\left(\frac{1}{m_1} + \frac{1}{m_2}\right) k_\perp (u\hat{\boldsymbol{u}} + w\hat{\boldsymbol{w}}) + (1 - \boldsymbol{n}\boldsymbol{n}^T) S (k_\perp u \hat{\boldsymbol{u}} + k_\perp w \hat{\boldsymbol{w}} + kn\hat{\boldsymbol{n}}), \end{aligned}$$

where S is given in (4). Comparing the last equation above with (40), we obtain the relative tangential motion of $\mathcal{B}_1$ to $\mathcal{B}_2$ in the case of sticking contact:

$$\ddot{u}\hat{\boldsymbol{u}} + \ddot{w}\hat{\boldsymbol{w}} = -\left(\frac{1}{m_1} + \frac{1}{m_2}\right) k_\perp (u\hat{\boldsymbol{u}} + w\hat{\boldsymbol{w}}) + (1 - \boldsymbol{n}\boldsymbol{n}^T) S (k_\perp u \hat{\boldsymbol{u}} + k_\perp w \hat{\boldsymbol{w}} + kn\hat{\boldsymbol{n}}). \tag{41}$$

This motion is decoupled when the inertia matrix S is diagonal. In such a case, let $\lambda_1, \lambda_2, \lambda_3$ be the entries on the diagonal of S. Then $\mathcal{B}_1$ undergoes harmonic motions relative to $\mathcal{B}_2$ in the tangent plane:[9]

$$\ddot{u} + \left(\frac{1}{m_1} + \frac{1}{m_2} - \lambda_1\right) k_\perp u = 0, \tag{42}$$

$$\ddot{w} + \left(\frac{1}{m_1} + \frac{1}{m_2} - \lambda_2\right) k_\perp w = 0. \tag{43}$$

Section 8.1 will offer an example of a ball striking a table.

4.4 Slip

Under slip, the tangential contact force $\boldsymbol{F}_\perp$ exerted on the u- and w-springs is due to sliding friction. It has two equivalent forms given in (33). We here determine the change rates $\dot{u}$ and $\dot{w}$ of the spring lengths for the purpose of updating the integrals G_u and G_w defined in (27) and (28), and E_u and E_w subsequently. Equation (35) relates $\dot{u}$ and $\dot{w}$ linearly in terms of u, w, and the contact velocity $\boldsymbol{v}$. To solve for $\dot{u}$ and $\dot{w}$, we need to set up a second equation. First, eliminate the normal contact force from (33) via substitution of (17):

$$k_\perp(u\hat{\boldsymbol{u}} + w\hat{\boldsymbol{w}}) = \mu \cdot \sqrt{2kE_n}\hat{\boldsymbol{v}}_s. \tag{44}$$

Take the dot products of both sides of this equation with themselves:

$$u^2 + w^2 = 2\mu^2 \frac{k}{k_\perp^2} E_n. \tag{45}$$

Combined with the last two equations in (16), the above equation relates the elastic energies stored by the three springs during slip:

$$E_u + E_w = \mu^2 \frac{k}{k_\perp} E_n = \mu^2 \eta^2 E_n. \tag{46}$$

Namely, the strain energy built up due to tangential compliance is a factor of that due to normal compliance: this factor depends on the ratio of the normal stiffness to the tangential stiffness, as well as the coefficient of contact friction.

Moving on, we differentiate (45) with respect to time:

$$u\dot{u} + w\dot{w} = \mu^2 \frac{k}{k_\perp^2} \dot{E}_n. \tag{47}$$

Equations (35) and (47) are in $\dot{u}$ and $\dot{w}$. The determinant of their coefficient matrix is $u^2 + w^2$. So a unique solution exists unless $u = w = 0$. Multiply (35) with w and (47) with u, and add them up to eliminate the terms involving $\dot{w}$:

$$(u^2 + w^2)\dot{u} = \mu^2 \frac{k}{k_\perp^2} \dot{E}_n u + v_u w^2 - v_w uw.$$

[9] As pointed out by Stronge (2000), the particle always undergoes a harmonic motion in the sticking mode of a 2-dimensional impact.

This yields

$$\begin{aligned}
\dot{u} &= \frac{\mu^2 \cdot \frac{k}{k_\perp^2} \cdot \dot{E}_n u + v_u w^2 - v_w uw}{u^2 + w^2} \\
&= \frac{\mu^2 \cdot \frac{k}{k_\perp^2} \cdot E_n' \cdot \dot{I}_n u + v_u w^2 - v_w uw}{u^2 + w^2} \\
&= \frac{\mu^2 \cdot \frac{k}{k_\perp^2} \cdot E_n' \cdot \sqrt{2kE_n} \cdot \alpha \sqrt{\frac{2E_u}{k_\perp}} + v_u \frac{2E_w}{k_\perp} - v_w \alpha\beta \cdot \frac{2}{k_\perp} \cdot \sqrt{E_u E_w}}{2\mu^2 \cdot \frac{k}{k_\perp^2} \cdot E_n} \\
& \qquad\qquad\qquad\qquad\qquad\qquad\qquad\qquad\qquad\qquad \text{by (17), (22), and (45)} \\
&= \frac{-\alpha\mu^2 \sqrt{\frac{k}{k_\perp}} \cdot v_n \sqrt{E_n E_u} + \frac{k_\perp}{k} v_u E_w - \alpha\beta \frac{k_\perp}{k} v_w \sqrt{E_u E_w}}{\mu^2 E_n} \qquad \text{by (18).}
\end{aligned}$$

With a substitution of (14) into the last equation above, we derive the change rate of the length of the u-spring:

$$\dot{u} = \frac{-\alpha\mu^2\eta^3 v_n \sqrt{E_n E_u} + v_u E_w - \alpha\beta v_w \sqrt{E_u E_w}}{\mu^2 \eta^2 E_n}, \tag{48}$$

Similarly, we obtain

$$\dot{w} = \frac{-\beta\mu^2\eta^3 v_n \sqrt{E_n E_w} + v_w E_u - \alpha\beta v_u \sqrt{E_u E_w}}{\mu^2 \eta^2 E_n}. \tag{49}$$

With $\dot{u}$ and $\dot{w}$, the contact sliding velocity $\boldsymbol{v}_s$ follows from (32).

Clearly, the change rates $\dot{u}$ and $\dot{w}$ of lengths of the two tangential springs are continuous within a contact mode. Continuity is maintained at a transition from slip to stick because the transition condition (37) holds during stick. However, discontinuity may happen at a transition from stick to slip. Even though the left derivatives $\dot{u}^- = v_u$ and $\dot{w}^- = v_w$ satisfy (52), there is no guarantee that (47) from differentiation of (46) holds. As a result, the right derivatives $\dot{u}^+$ and $\dot{w}^+$ as solution to (35) and (47) may be different from the left derivatives. An example of this discontinuity will be given later in Figure 12(b) resulting from a ball-table collision.

4.5 Contact Mode Detection and Transition

Under Coulomb's law of friction, the contact between the two impacting bodies sticks if $\sqrt{F_u^2 + F_w^2} < \mu F_n$, namely,

$$\sqrt{\dot{I}_u^2 + \dot{I}_w^2} < \mu \dot{I}_n. \tag{50}$$

By equations (17), (19), and (20), comparing $\sqrt{F_u^2 + F_w^2}$ with μF_n is equivalent to comparing $E_u + E_w$ and $\mu^2\eta^2 E_n$. Thus, the contact sticks if

$$E_u + E_w < \mu^2 \eta^2 E_n. \tag{51}$$

When $\sqrt{F_u^2 + F_w^2} = \mu F_n$, i.e.,

$$E_u + E_w = \mu^2 \eta^2 E_n, \tag{52}$$

the contact sticks if the sliding velocity $\boldsymbol{v}_s$ vanishes, and slips otherwise. By (32), vanishing of $\boldsymbol{v}_s$ happens when

$$\boldsymbol{v}_\perp = \dot{u}\hat{\boldsymbol{u}} + \dot{w}\hat{\boldsymbol{w}}, \tag{53}$$

where $\dot{u}$ and $\dot{w}$ are given in (48) and (49), respectively, in terms of the strain energies.

If (51) holds, or (52) and (53) both hold, the contact sticks. Otherwise, it slips.

The strain energies E_u and E_w do not change their values at the contact mode switch. At the end of compression, the value of $\mu^2\eta^2 E_n$ does not change because $\eta^2 = k/k_\perp$ increases from η_0^2 to η_0^2/e^2 while E_n reduces to a factor of e^2 of its value under the impact law.

4.6 Initial Contact Mode

We first hypothesize that the impact starts with the sticking contact, and derive a condition on the initial contact velocity $\boldsymbol{v}_0$ equivalent to that stated in Coulomb's law. If the condition is satisfied (and thus consistent with the hypothesis), initial stick occurs. Otherwise, initial slip occurs. Under Coulomb's law, stick happens at the beginning if

$$\lim_{\Delta t\to 0} \frac{\|\dot{I}_u\hat{\boldsymbol{u}} + \dot{I}_w\hat{\boldsymbol{w}}\|}{\dot{I}_n} \le \mu, \tag{54}$$

and slip happens otherwise.

We here look at an infinitesimal amount of time Δt after the impact begins. The value of $\dot{I}_u$, i.e., the force F_u on the u-spring, is

$$\begin{aligned} \dot{I}_u &= -k_\perp u = -k_\perp \int_0^{\Delta t} \dot{u}\, dt \\ &= -k_\perp \int_0^{\Delta t} v_u\, dt, \quad \text{by (38)}. \end{aligned}$$

Similarly, we obtain

$$\begin{aligned} \dot{I}_w &= -k_\perp \int_0^{\Delta t} v_w\, dt, \\ \dot{I}_n &= -k_0 \int_0^{\Delta t} v_n\, dt. \end{aligned}$$

Recall the initial velocity $\boldsymbol{v}_0 = v_{0u}\hat{\boldsymbol{u}} + v_{0w}\hat{\boldsymbol{w}} + v_{0n}\hat{\boldsymbol{n}}$ with $v_{0w} = 0$. With $\dot{I}_u$, $\dot{I}_w$, and $\dot{I}_n$, the limit in (54) is determined:

$$\begin{aligned} \lim_{\Delta t\to 0} \frac{\|\dot{I}_u\hat{\boldsymbol{u}} + \dot{I}_w\hat{\boldsymbol{w}}\|}{\dot{I}_n} &= \lim_{\Delta t\to 0} \frac{\|\int_0^{\Delta t}(v_u\hat{\boldsymbol{u}} + v_w\hat{\boldsymbol{w}})\, dt\|}{-\int_0^{\Delta t} v_n\, dt} \cdot \frac{k_\perp}{k_0} \\ &= \lim_{\Delta t\to 0} \frac{\int_0^{\Delta t}\sqrt{v_u^2 + v_w^2}\, dt}{-\int_0^{\Delta t} v_n\, dt} \cdot \frac{1}{\eta_0^2} \\ &= \frac{\sqrt{v_{0u}^2 + v_{0w}^2}}{-v_{0n}} \cdot \frac{1}{\eta_0^2} \qquad \text{by L'Hospital's rule} \\ &= \frac{v_{0u}}{v_{0n}\eta_0^2}. \end{aligned}$$

The second equation above follows from that $\boldsymbol{v}$ does not vary its direction over $[0, \Delta t]$ as $\Delta t \to 0$. The last one follows from the choice of $\hat{\boldsymbol{u}}$. Note that $v_{0u}^2 = (\boldsymbol{v}_0 \cdot \boldsymbol{v}_0)^2 - v_{0n}^2$. Substitution of the last equation above into (54) yields conditions for initial slip and stick, as stated below.

Proposition 1 *The impact starts with a sticking contact if*

$$\|\boldsymbol{v}_0\| \leq -\sqrt{1+\mu^2\eta_0^4} \cdot (\boldsymbol{v}_0 \cdot \hat{\boldsymbol{n}}), \tag{55}$$

or a sliding contact if

$$\|\boldsymbol{v}_0\| > -\sqrt{1+\mu^2\eta_0^4} \cdot (\boldsymbol{v}_0 \cdot \hat{\boldsymbol{n}}). \tag{56}$$

Appendix 9 will derive the initial values of the ratios of the strain energies E_u and E_w stored by the tangential springs to that stored by the normal spring, as follows:

$$\lim_{I_n \to 0} \frac{E_u}{E_n} = \begin{cases} \left(\dfrac{v_{0u}}{\eta_0 v_{0n}}\right)^2, & \text{if stick,} \\ \mu^2\eta_0^2, & \text{if slip;} \end{cases} \tag{57}$$

$$\lim_{I_n \to 0} \frac{E_w}{E_n} = 0. \tag{58}$$

The energy ratios for initial slip are plugged into (48) and (49) to determine the corresponding initial change rates $\dot{u}$ and $\dot{w}$ of the lengths of the two tangential springs. The rates $\dot{u}$ and $\dot{w}$ in the case of initial stick easily follow from (38) and (39) and that the tangential contact velocity initially opposes $\hat{\boldsymbol{u}}$. Combine the expressions for the two contact modes:

$$\dot{u}(0) = \begin{cases} v_{0u}, & \text{if stick,} \\ \mu\eta_0^2 v_{0n}, & \text{if slip;} \end{cases} \tag{59}$$

$$\dot{w}(0) = 0. \tag{60}$$

The ratios (57) and (58) are also plugged into (23) and (24) to obtain the initial impulse derivatives (with $\alpha = -1$ and $\eta = \eta_0$):

$$I_u'(0) = \begin{cases} \dfrac{v_{0u}}{\eta_0^2 v_{0n}}, & \text{if stick,} \\ \mu, & \text{if slide;} \end{cases} \tag{61}$$

$$I_w'(0) = 0. \tag{62}$$

5 Impact System of Differential Equations

It is time to summarize the system of equations that governs two-body impact with tangential compliance. The impact outcome (1) is determined by the impulse $\boldsymbol{I}$ exerted by the lower body $\mathcal{B}_2$ on the upper body $\mathcal{B}_1$. The contact velocity follow from (3) and (13):

$$\boldsymbol{v} = v_u\hat{\boldsymbol{u}} + v_w\hat{\boldsymbol{w}} + v_n\hat{\boldsymbol{n}} = \boldsymbol{v}_0 + \left(\frac{1}{m_1} + \frac{1}{m_2}\right)\boldsymbol{I} - S\boldsymbol{I}, \tag{63}$$

where $\boldsymbol{v}_0$ is the initial contact velocity (2) determined from the objects' pre-impact velocities, and S is the 3×3 matrix given in (4).

The impulse is $\boldsymbol{I} = I_n\hat{\boldsymbol{n}} + I_u\hat{\boldsymbol{u}} + I_w\hat{\boldsymbol{w}}$, where the normal impulse I_n is an independent variable for the impact, and the tangential impulses I_u and I_w are functions whose derivatives are, from (23) and (24),

$$I_u' = -\frac{\alpha}{\eta}\sqrt{\frac{E_u}{E_n}} \qquad \text{and} \qquad I_w' = -\frac{\beta}{\eta}\sqrt{\frac{E_w}{E_n}}. \tag{64}$$

Here α and β, defined in (21), are two-value variables indicating whether the two tangential springs extend or compress, respectively. The strain energy stored by the normal spring varies at the rate:

$$E_n' = \boldsymbol{v} \cdot \hat{\boldsymbol{n}} = -v_n. \tag{65}$$

It loses a factor $1 - e^2$ of its value at the end of compression. The strain energies stored by the tangential springs are copied over from (30) and (31) as

$$E_u = \frac{G_u^2}{4\eta_0^2}, \qquad \text{and} \qquad E_w = \frac{G_w^2}{4\eta_0^2}, \tag{66}$$

where the two integrals G_u and G_w respectively record changes u and w in lengths of the u- and w-springs up to a constant factor. Their derivatives with respect to I_n are

$$\begin{cases} G_u' = \dfrac{\dot{u}}{\sqrt{E_n}} \quad \text{and} \quad G_w' = \dfrac{\dot{w}}{\sqrt{E_n}}, & \text{if compression,} \\ G_u' = e\dfrac{\dot{u}}{\sqrt{E_n}} \quad \text{and} \quad G_w' = e\dfrac{\dot{w}}{\sqrt{E_n}} & \text{if restitution,} \end{cases} \tag{67}$$

where the rates $\dot{u}$ and $\dot{w}$ depend on the contact mode, and after merging (38) with (48) and (39) with (49), are

$$\dot{u} = \begin{cases} v_u, & \text{if stick,} \\ \dfrac{-\alpha\mu^2\eta^3 v_n\sqrt{E_nE_u} + v_uE_w - \alpha\beta v_w\sqrt{E_uE_w}}{\mu^2\eta^2E_n}, & \text{if slip;} \end{cases} \tag{68}$$

$$\dot{w} = \begin{cases} v_w, & \text{if stick,} \\ \dfrac{-\beta\mu^2\eta^3 v_n\sqrt{E_nE_w} + v_wE_u - \alpha\beta v_u\sqrt{E_uE_w}}{\mu^2\eta^2E_n}, & \text{if slip.} \end{cases} \tag{69}$$

To put the above equations into the standard form of a system of ordinary differential equations, we first substitute (63) for $\boldsymbol{v}$ in (65). Then substitute (63) for $\boldsymbol{v}$ and (66) for E_u and E_w into (68) and (69). Next, substitute the resulting expressions for $\dot{u}$ and $\dot{w}$ in (67), respectively. In the resulting expressions for G_u' and G_w', and in the expressions (64) for I_u' and I_w', replace the occurrences of E_u and E_w with their expressions (66). Having eliminated the occurrences of E_u, E_w, v_u, v_w, and v_n, we end up with a system of five differential equations involving one variable I_n and five functions I_u, I_w, G_u, G_w, and E_n:

$$\begin{aligned} I_u' &= f_1(E_n, G_u), \\ I_w' &= f_2(E_n, G_w), \\ G_u' &= f_3(I_n, E_n, G_u, G_w), \\ G_w' &= f_4(I_n, E_n, G_u, G_w), \\ E_n' &= f_5(I_n, I_u, I_w). \end{aligned} \tag{70}$$

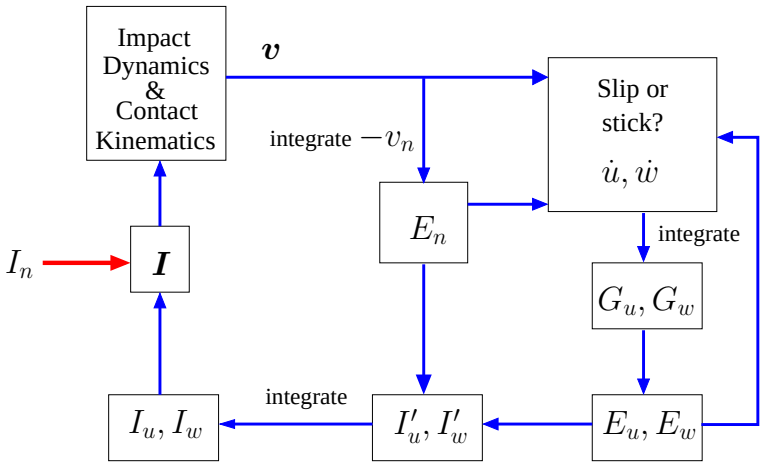

Figure 8: Diagram for impulse computation.

In the above, f_i, $1 \le i \le 5$ are the functions that result from the aforementioned substitution steps. The computation is *energy-based* because G_u and G_w essentially represent E_u and E_w.

Figure 8 is a flow chart for the impact system that expands the diagram in Figure 3. The system finishes at the end of restitution of the normal impact. As I_n accumulates independently, the normal impact ends compression when $\dot{n} = 0$, suffering a loss of the strain energy E_n by a factor of $1 - e^2$, and then releases the remaining amount of E_n during restitution. In the loop, the motions of the two objects are updated using the total impulse $\boldsymbol{I}$. The contact velocity $\boldsymbol{v}$ is updated accordingly, so is the energy E_n stored by the normal spring. Meanwhile, the contact mode is determined using $\boldsymbol{v}$, E_u, E_w, and E_n. Increments are added to the integrals G_u and G_w to track the changes in length of the two tangential springs. From G_u and G_w, E_u and E_w are computed. Afterward, the derivatives of the tangential impulses I_u and I_w with respect to the normal impulse I_n are obtained, and integrated. The three impulses I_u, I_w, and I_w are assembled into $\boldsymbol{I}$ to close the loop.

In the right hand sides of equations (63)–(69), only E_n among the five functions appears in the denominators. Thus, in the system (70) derived from them, only E_n appears in the denominators in the functions f_i, $1 \le i \le 5$. During the impact, $E_n > 0$. That $\dot{u}$, $\dot{w}$, G'_u, and G'_w are piecewise continuous functions does not affect their integrability. So f_i, $1 \le i \le 5$, in (70) are piecewise continuous in I_u, I_w, G_u, G_w and E_n. Their integrals, i.e., the values of I_u, I_w, G_u, G_w, E_n are unique as long as $E_n \neq 0$. In the below we establish that the solution uniquely exists at the beginning of the impact. Then the impact model generates a unique outcome.

The initial values are

$$I_u(0) = I_w(0) = 0, \qquad G_u(0) = G_w(0) = 0, \qquad \text{and} \qquad E_n(0) = 0. \tag{71}$$

From (65), we have that

$$E'_n(0) = -v_{0n}. \tag{72}$$

The initial values of the derivatives I'_u and I'_w are given in (61) and (62). Appendix 9 establishes

Algorithm 1 Impact with Tangential Compliance

1: initialization
2: $\Delta I_n \leftarrow \delta$
3: **while** not end of restitution **do**
4: evaluate $\dot{u}$ and $\dot{v}$ according to (68) and (69) given the present contact mode
5: evaluate G'_u and G'_w according to (67) given the present impact phase
6: $G_u \leftarrow G_u + G'_u \Delta I_n$
7: $G_w \leftarrow G_w + G'_w \Delta I_n$
8: update E_u and E_w according to (30) and (31), respectively.
9: $E_n \leftarrow E_n - v_n \Delta I_n$ by (18)
10: evaluate I'_u and I'_w according to (64)
11: $\boldsymbol{I} \leftarrow \boldsymbol{I} + (I'_u \hat{\boldsymbol{u}} + I'_w \hat{\boldsymbol{w}} + \hat{\boldsymbol{n}}) \cdot \Delta I_n$
12: update $\boldsymbol{v}$ according to (63)
13: **if** contact sticks and $E_u + E_w = \mu^2 \eta^2 E_n$ **then**
14: switch to slip
15: **end if**
16: **if** contact slips and $\boldsymbol{v}_\perp = \dot{u}\hat{\boldsymbol{u}} + \dot{w}\hat{\boldsymbol{w}}$ **then**
17: switch to stick
18: **end if**
19: **if** compression and $v_n = 0$ **then**
20: compression ends
21: **end if**
22: **if** restitution and $E_n = 0$ **then**
23: restitution ends
24: **end if**
25: **end while**
26: update $\boldsymbol{V}_i$ and $\boldsymbol{\omega}_i$, $i = 1, 2$ using $\boldsymbol{I}$ according to impact equations (1)

that for I_n small enough,

$$G_u = \begin{cases} \frac{2v_{0u}}{\sqrt{-v_{0n}}}\sqrt{I_n} + O(I_n^{3/2}), & \text{if initial stick,} \\ -2\mu\eta_0^2\sqrt{-v_{0n} I_n} + o(\sqrt{I_n}), & \text{if initial slip;} \end{cases} \tag{73}$$

$$G_w = O(I_n^{3/2}). \tag{74}$$

In the above, the Big-O and small-o notation are used such that $O(I_n^{3/2}) < cI_n^{3/2}$ for some constant c and all small enough values of I_n, and $\lim_{I_n \to 0} o(\sqrt{I_n})/\sqrt{I_n} = 0$. We see that the initial changes in I_u, I_w, G_u, G_w, and E_n are determined.

The system (70) does not have a closed-form solution in general. We need to carry out numerical integration over I_n with a small step size, say, δ. The pseudo-code is given in Algorithm 1, which outputs the total impulse $\boldsymbol{I}$, and computes the post-impact velocities of the two bodies.

Line 1 initializes function values given in (71) for integration. The initial contact mode is determined according to Proposition 1. To avoid numerical instability, we start numerical integration at $I_n = 0$.

In the first integration step, E_n, I_u, I_w are approximated using their first order Taylor series

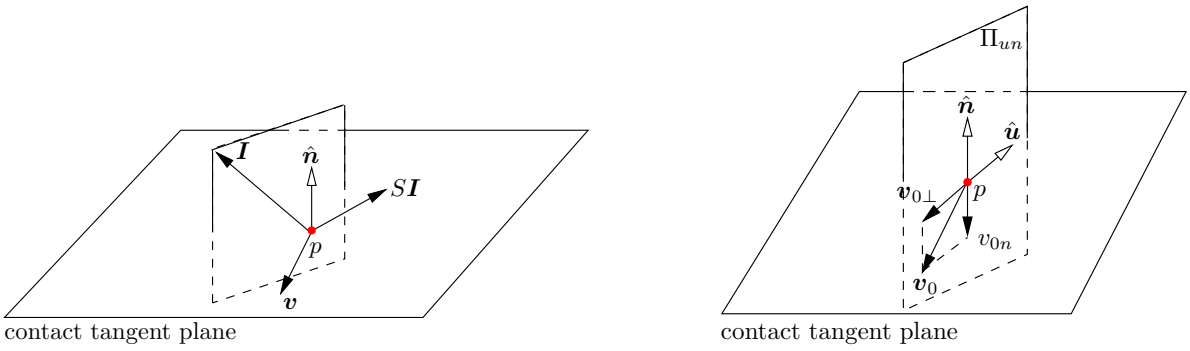

Figure 9: (a) Generally non-coplanar contact velocity $\boldsymbol{v}$, impulse $\boldsymbol{I}$, and contact normal $\hat{\boldsymbol{n}}$ during the impact; and (b) normal plane Π_{un} spanned by $\hat{\boldsymbol{n}}$ and the initial contact velocity $\boldsymbol{v}_0$.

about 0 with the derivatives given in (72), (61), (62). The value of $G_u(\delta)$ is approximated using (73) by ignoring the Big-O term. We also let $G_w(\delta) = 0$ since it can be ignored in comparison with $G_u(\delta)$.

Lines 3–25 is the main loop that simulates the physical impact process, incrementally updating the contact strain energy components, the impulse, and the contact velocity. These lines also keep track of contact modes and impact phases. The algorithm fills in the details missing from the diagram in Figure 8.

6 Planar Impact

From (5), the tangential velocity $\boldsymbol{v}_\perp$ often changes along a direction different than the tangential impulse $\boldsymbol{I}_\perp$ does, because $(1 - \boldsymbol{n}\boldsymbol{n}^T)S\boldsymbol{I}$, the projection of $S\boldsymbol{I}$ onto the contact plane, is rarely collinear with $\boldsymbol{I}_\perp$. As a result, the impulse $\boldsymbol{I}$ generally grows along a space curve (see Figure 9(a)). Only for objects with special geometry in certain impact configurations will $S\boldsymbol{I}$ be a linear combination of the normal $\hat{\boldsymbol{n}}$ and $\boldsymbol{I}$. Recall the definition (12) of the unit tangent vector $\hat{\boldsymbol{u}}$, and denote by Π_{un} the normal plane spanned by $\hat{\boldsymbol{u}}$ and $\hat{\boldsymbol{n}}$.

Theorem 2 *A planar impact occurs in one of the following two situations:*

i) When $\boldsymbol{v}_0 \times \hat{\boldsymbol{n}} \neq 0$ or $\boldsymbol{n}$ is not an eigenvector of the matrix S defined in (4), the impulse $\boldsymbol{I}$ lies in the plane Π_{un} throughout the impact if $S\hat{\boldsymbol{u}} \in \Pi_{un}$ and $S\hat{\boldsymbol{n}} \in \Pi_{un}$.

ii) When $\boldsymbol{v}_0 \times \hat{\boldsymbol{n}} = 0$ and $\hat{\boldsymbol{n}}$ is an eigenvector of S, $\boldsymbol{I}$ is along $\hat{\boldsymbol{n}}$; that is, the impact is a direct impact.

Proof We prove i) first. Consider that either $\boldsymbol{v}_0 \times \hat{\boldsymbol{n}} \neq 0$ or $\boldsymbol{n}$ is not an eigenvector of S. Suppose $S\hat{\boldsymbol{u}}, S\hat{\boldsymbol{n}} \in \Pi_{un}$. Then $S\boldsymbol{x} \in \Pi_{un}$ for any $\boldsymbol{x} \in \Pi_{un}$ because S is a linear map. Note that $v_{0n} = \boldsymbol{v}_0 \cdot \hat{\boldsymbol{n}} < 0$ for the impact to happen. Below we establish three invariants related to the $\hat{\boldsymbol{w}}$ direction during the impact:

$$v_w = 0, \qquad G_w = 0, \qquad \text{and} \qquad I_w = 0. \tag{75}$$

They are clearly true at the start. So we just need to show that, whenever (75) holds, the derivatives of these functions vanish, i.e,

$$v'_w = 0, \qquad G'_w = 0, \qquad \text{and} \qquad I'_w = 0. \tag{76}$$

Then v_w, G_w, and I_w must be identically zero during the impact.

We first prove that (76) is true at the start of the collision. Under Coulomb's law, the frictional force must be opposite to $\boldsymbol{v}_{0\perp}$. That $I'_w(0) = 0$ is by (62). We differentiating (74) with respect to I_n and obtain $G'_w = O(\sqrt{I_n})$. Thus, $G'_w(0) = 0$.

To establish zero initial value of v'_w, we differentiate (63) and then take the dot product with $\hat{\boldsymbol{w}}$:

$$v'_w = \boldsymbol{v}' \cdot \hat{\boldsymbol{w}} = \left(\frac{1}{m_1} + \frac{1}{m_2}\right) I'_w - (S\boldsymbol{I}') \cdot \hat{\boldsymbol{w}} \tag{77}$$

Since $I'_w = 0$, $\boldsymbol{I}'$ lies in the plane Π_{un} initially. Therefore, $S\boldsymbol{I}' \in \Pi_{un}$ under the condition that $S\boldsymbol{x} \in \Pi_{un}$ for any $\boldsymbol{x} \in \Pi_{un}$. This implies $(S\boldsymbol{I}') \cdot \hat{\boldsymbol{w}} = 0$. So we have $v'_w(0) = 0$.

Next, we show that the invariants in (76) hold if those in (75) do during the collision where $I_n > 0$ and thus $E_n > 0$. First, $G_w = 0$ directly implies $E_w = 0$ by (66). Substitutions of (57), (58), and $v_w = 0$ into (69) yield $\dot{w} = 0$ in both possible contact modes. Then $G'_w = 0$ follows from (67). Meanwhile, $I'_w = 0$ follows from (64) and (58). Finally, $v'_w = 0$ follows from (77), $I'_w = 0$, and that $\boldsymbol{I}'(0)$ and $S\boldsymbol{I}'(0) = S(\hat{\boldsymbol{n}} + I'_u\hat{\boldsymbol{u}})$ lie in the plane Π_{un}.

Next, let us prove ii). Suppose $\boldsymbol{v}_0 \times \hat{\boldsymbol{n}} = 0$ and $\hat{\boldsymbol{n}}$ is an eigenvector of S. The contact sticks initially. Let λ be the corresponding eigenvalue. Namely, $S\hat{\boldsymbol{n}} = \lambda\hat{\boldsymbol{n}}$. Equation (63) becomes

$$\boldsymbol{v} = \boldsymbol{v}_0 + \left(\frac{1}{m_1} + \frac{1}{m_2} - \lambda\right) \boldsymbol{I}.$$

Differentiate the above:

$$\boldsymbol{v}' = \left(\frac{1}{m_1} + \frac{1}{m_2} - \lambda\right) \boldsymbol{I}'. \tag{78}$$

Since $\boldsymbol{v}_0$ is collinear with $\hat{\boldsymbol{n}}$, $v_{0u} = v_{0w} = 0$. Thus, $I'_u(0) = I'_w(0) = 0$ by (61) and (62), and $\boldsymbol{I}'(0) = \hat{\boldsymbol{n}}$. Equation (78) implies that $\boldsymbol{v}$ and $\boldsymbol{I}$ are collinear with $\hat{\boldsymbol{n}}$ during the impact. □

Does $\boldsymbol{I} \in \Pi_{un}$ imply $S\hat{\boldsymbol{u}}, S\hat{\boldsymbol{w}} \in \Pi_{un}$? From (3), we see that $\boldsymbol{I}$ lies in Π_{un} if and only if $S\boldsymbol{I}$ does. Meanwhile, $S\boldsymbol{I} \in \Pi_{un}$ as $\boldsymbol{I}$ grows if $S\hat{\boldsymbol{u}}, S\hat{\boldsymbol{n}} \in \Pi_{un}$. The latter condition is almost always true given $\boldsymbol{I} \in \Pi_{un}$. This is because as long as $\boldsymbol{I}$ does not grow along a line, two of its intermediate values span Π_{un}. The condition $S\hat{\boldsymbol{u}}, S\hat{\boldsymbol{n}} \in \Pi_{un}$ in part i) of Theorem 2 is often necessary too.

7 Impact Scalability

One important property of an impact model is scalability. More specifically, if the velocities of the two bodies before they collide scale by a factor s, their velocities after the collision should scale by the same factor. Let us refer to the original collision instance, with velocities $(\boldsymbol{V}_1, \boldsymbol{\omega}_1)$ and $(\boldsymbol{V}_2, \boldsymbol{\omega}_2)$, as A, while the instance with scaled velocities $(s\boldsymbol{V}_1, s\boldsymbol{\omega}_1)$ and $(s\boldsymbol{V}_2, s\boldsymbol{\omega}_2)$ as B. All terms related to impact A are denoted by the same symbols as before.

Theorem 3 *A one-to-one correspondence exists between a moment during impact A determined by the normal impulse value I_n and a moment during impact B determined by the normal impulse value sI_n such that the following hold in B at the moment:*

i) The velocities of the two colliding bodies are $s\boldsymbol{V}_i$ and $s\boldsymbol{\omega}_i$, $i = 1, 2$.

ii) The strain energies of the three virtual springs are s^2E_n, s^2E_u, s^2E_w.

iii) The rates of changes in length of the two tangential springs are $s\dot{u}$ and $s\dot{w}$.

iv) Their changes in length are $sG_u/\sqrt{2k_0}$ and $sG_w/\sqrt{2k_0}$.

v) The impulse derivatives I'_u and I'_w have the same values as in A.

Proof Suppose in instance A, the terms $\boldsymbol{I}$, $\boldsymbol{v}$, $\boldsymbol{\omega}$, E_n, E_u, E_w, G_u, and G_w constitute the solution to the system (70). We substitute the scaled terms $s\boldsymbol{I}, s\boldsymbol{v}, s\boldsymbol{\omega}$, s^2E_n, s^2E_u, s^2E_w, sG_u, and sG_w respectively for occurrences of these terms in the system. Note that $E'_n = v_n$ is scaled by s. It is not hard to verify that the resulting system of equations still hold. For instance, in (68), its left hand side is replaced by $s\dot{u}$. Its right hand side, in the case of sticking contact, becomes sv_u; and in the case of slipping contact, becomes

$$\begin{aligned} & \frac{-\alpha\mu^2\eta^3(sv_n)\sqrt{s^4E_nE_u} + (sv_u)s^2E_w - \alpha\beta(sv_w)\sqrt{s^4E_uE_w}}{\mu^2\eta^2s^2E_n} \\ = \quad & s \cdot \frac{-\alpha\mu^2\eta^3v_n\sqrt{E_nE_u} + v_uE_w - \alpha\beta v_w\sqrt{E_uE_w}}{\mu^2\eta^2E_n}. \end{aligned}$$

Hence, the right hand side is also scaled by s in either contact mode. Equation (68) still holds.

The theorem then follows from the uniqueness of the solution to the system of differential equations. □

8 Examples

This section applies the impact model with tangential compliance to two collisions with a table — one by a ball and the other by a pencil. The two instances are representative in that they yield planar and space impulse curves, respectively.

8.1 Ball-Table Collision

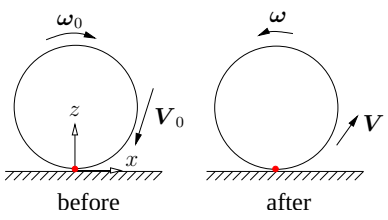

Figure 10: Ball striking a table.

Cross (2010) investigated frictional impact of a ball on a cart, modeling tangential compliance by allowing the cart, attached to a vertical wall via a spring at one end, to translate horizontally. His analysis was performed in time space in a way similar to Stronge's [59] with simulation results showing a range of spins of the rebounding ball.

Here we treat a ball-table impact in impulse space using the introduced compliance model. As shown in Figure 10, a ball with initial velocity $\boldsymbol{V}_0$ and angular velocity $\boldsymbol{\omega}_0$ strikes a still table. Let r be the ball's radius and m its mass.

Hence its angular inertia is $\frac{2}{5}mr^2$. Denote by $\boldsymbol{z}$ the upward contact normal, and $\boldsymbol{I}$ the impulse exerted by the table on the ball during the collision. Dynamics yield the following velocity equations:

$$\boldsymbol{V} = \boldsymbol{V}_0 + \frac{\boldsymbol{I}}{m} \quad \text{and} \quad \boldsymbol{\omega} = \boldsymbol{\omega}_0 - \frac{5}{2mr}\boldsymbol{z} \times \boldsymbol{I}, \tag{79}$$

where the normal component I_z of the impulse $\boldsymbol{I}$ is the only variable for the impact system.

The vector $\boldsymbol{r} = (0, 0, -r)^T$ locates the contact point relative to the ball's center. We substitute (79) into the contact velocity $\boldsymbol{v} = \boldsymbol{V} + r\hat{\boldsymbol{z}} \times \boldsymbol{\omega}$, and, after several steps, obtain

$$\boldsymbol{v} = \boldsymbol{v}_0 + \Delta\boldsymbol{v}, \tag{80}$$

where $\boldsymbol{v}_0 = \boldsymbol{V}_0 + r\hat{\boldsymbol{z}} \times \boldsymbol{\omega}_0$ is the initial contact velocity, and

$$\Delta\boldsymbol{v} == \frac{1}{m}\boldsymbol{I} - S\boldsymbol{I}. \tag{81}$$

with

$$S = -\frac{5}{2m}\begin{pmatrix} 1 & 0 & 0 \\ 0 & 1 & 0 \\ 0 & 0 & 0 \end{pmatrix}. \tag{82}$$

We place the origin at the contact point, and choose the x-axis to oppose $\boldsymbol{v}_{0\perp}$, or, if $\boldsymbol{v}_{0\perp} = 0$, to be an arbitrary tangent vector. The x-y-z frame is identified with the n-u-w contact frame for tangential impulse in Section 3. Since $S\boldsymbol{x}, S\boldsymbol{z} \in \Pi_{xz}$, under Theorem 2 the impulse curve $\boldsymbol{I}$ stays in the plane Π_{xz} determined by $\boldsymbol{n}$ and $\boldsymbol{v}_0$, and is along $\hat{\boldsymbol{n}}$ if $\boldsymbol{v}_0 \times \hat{\boldsymbol{n}} = 0$. The impact is planar.

In all simulations in this section, we consider $r = 1$, and set the coefficient of friction, the coefficient of restitution, and compliance[10] as follows:

$$\mu = 0.4, \qquad e = 0.5, \qquad \text{and} \qquad \eta_0 = \sqrt{17/14}. \tag{83}$$

8.1.1 Impulse Curve

From (80) and (81) the tangential contact velocity is linear in the tangential impulse:

$$\boldsymbol{v}_\perp = \boldsymbol{v}_{0\perp} + \frac{7}{2m}\boldsymbol{I}_\perp. \tag{84}$$

Consider $\boldsymbol{V}_0 = (V_{0x}, V_{0y}, V_{0z}) = (-1, 0, -5)^T$ and $\boldsymbol{\omega}_0 = (0, 2, 0)^T$, which yields tangential contact velocity $\boldsymbol{v}_{0\perp} = (-3, 0, 0)^T$. We use Algorithm 1 to simulate the collision with the step size $\delta = 0.00005$. After the collision, the ball bounces backward with a reversal of its rotation:

$$\begin{aligned} \boldsymbol{V} &= (V_x, 0, V_z)^T = (0.570982, 0, 2.5)^T, \\ \boldsymbol{\omega} &= (0, \omega_y, 0)^T = (0, -1.92746, 0)^T. \end{aligned}$$

The scenario is captured in Figure 1(a)–(c). The ball's total energy has decreased from 13.4 to 3.65997. Of the energy loss, $\frac{1}{2}((-5)^2 - 2.5^2) = 9.375$ was due to irreversible deformation caused by the normal impact and characterized by the coefficient of restitution. The rest of the loss was due to contact friction.

[10] For a circular punch on a half space (Johnson 1985, pp. 361–366), this value of η_0 is derived from Poisson's ratio of the ball $\nu = 0.3$ under $\eta_0^2 = (2 - \nu)/(2 - 2\nu)$.

Figure 11 plots the impulse curve, on which the blue and black dots mark the ends of compression and restitution, respectively, and the two green dots mark contact mode transitions. The impact starts with a slip, changes from slip to stick at $I_z = 0.62485$, ends compression at $I_z = -mV_{0z} = 5$, starts a reverse slip at $I_z = 7.36575$, and ends restitution at $I_z = -(1+e)mV_{0z} = 7.5$.

During the impact, the tangential contact velocity and spring velocity, aligned with the x-axis, are denoted as scalars $v_\perp$ and $\dot{x}$, respectively. As shown in Figure 12(a), $v_\perp$ starts at -3 and ends at 2.49847. The rate $\dot{x}$ increases from -2.42852 with I_z until it equals $v_\perp$ at -2.12528, when the contact switches from slip to stick. The contact stays in stick with $\dot{x} = v_\perp$ until $I_z = 7.36575$ when a slip reversal happens. Figure 12(b) shows a sudden change of $\dot{x}$ from 2.59255 to -2.29806 at this moment. To see why, note that under slip, $\dot{x}$ must satisfy (47), which becomes $x\dot{x} = (\mu^2 k/k_\perp^2)\dot{E}_z$. Because the transition happens during restitution, the strain energy E_z stored by the normal spring is decreasing. So $\dot{E}_z < 0$, and x and $\dot{x}$ must have opposite signs at the moment. However, as seen from Figure 12(b) and (c), both $\dot{x}$ and x were positive before the slip reversal. Hence the sudden change in $\dot{x}$.

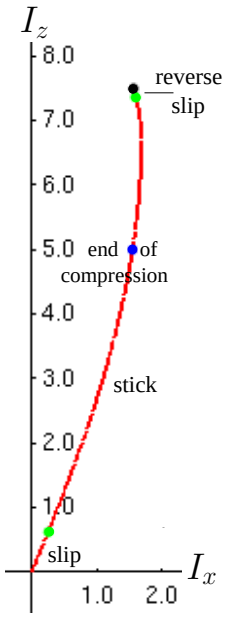

Figure 11: Impulse.

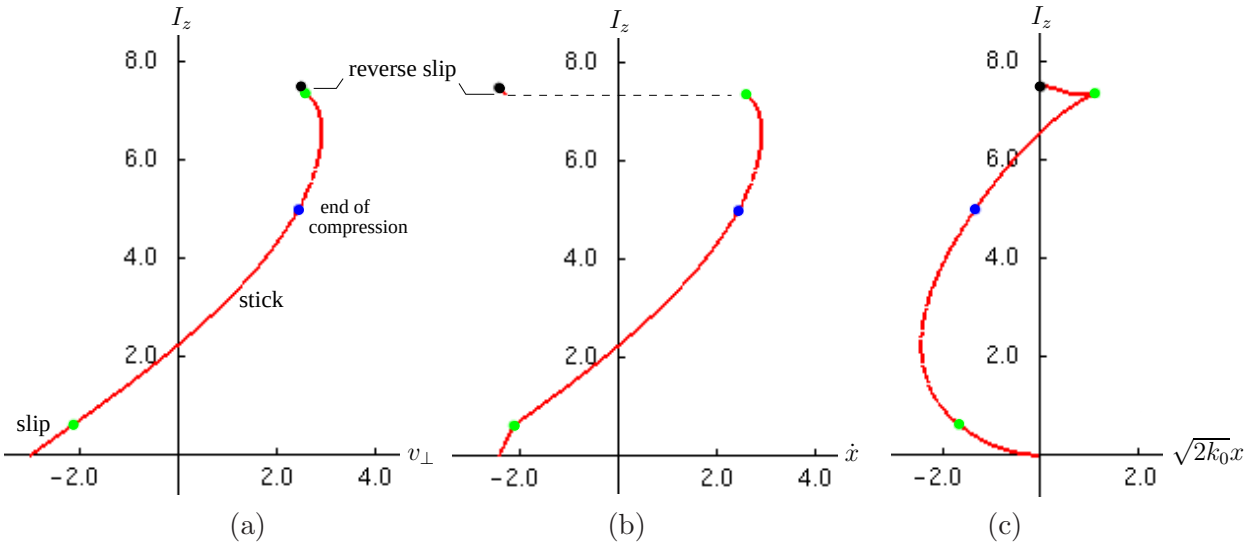

Figure 12: Evolutions of (a) tangential contact velocity, (b) rate of change in length of the x-spring, and (c) spring length x scaled by $\sqrt{2k_0}$. The dashed line in (b) marks a discontinuity as reverse slip happens.

The matrix S in (82) has one eigenvalue $-5/2m$. During stick the massless particle at the contact and attached to the x- and y-springs performs a harmonic motion from (42):[11]

$$\ddot{x} + \frac{7}{2m} k_\perp x = 0,$$

while $y = 0$.

[11] Here $m_2 = \infty$ and $\lambda_1 = -5/2$.

i	$\boldsymbol{V}_{2i-1}$	$\boldsymbol{\omega}_{2i-1}$
1	$(0.898172, -1.627, 2.5001)$	$(1.93249, 1.25457, 0)$
2	$(1.07389, -1.77762, 1.2501)$	$(1.55595, 0.815269, 0)$
3	$(0.944485, -1.6667, 0.62505)$	$(1.83325, 1.13879, 0)$
4	$(1.04364, -1.75169, 0.3123)$	$(1.62078, 0.890907, 0)$
5	$(0.963345, -1.68287, 0.15565)$	$(1.79283, 1.09164, 0)$
6	$(1.02677, -1.73723, 0.07665)$	$(1.65692, 0.933078, 0)$
7	$(0.998039, -1.7126, 0.0358)$	$(1.71849, 1.0049, 0)$
8	$(1.00197, -1.71598, 0.0111)$	$(1.71006, 0.995071, 0)$

Table 1: Velocities and angular velocities of a ball immediately after eight consecutive bounces. The ball velocities just before the first bounce are $\boldsymbol{V}_0 = (-1, 0, -5)^T$ and $\boldsymbol{\omega}_0 = (6, 6, 0)^T$.

8.1.2 Consecutive Bounces

Next, we simulate a sequence of consecutive bounces of the ball on the table triggered by an initial strike. For $i \geq 1$, denote by $\boldsymbol{V}_{2i-2}$ and $\boldsymbol{\omega}_{2i-2}$ the velocity and angular velocity immediately before the ith bounce, and by $\boldsymbol{V}_{2i-1}$ and $\boldsymbol{\omega}_{2i-1}$ the velocities immediately after the ith bounce. The ball has velocities $\boldsymbol{V}_0$ and $\boldsymbol{\omega}_0$ before the initial strike. Between the ith and $(i+1)$-st impacts the ball undergoes a free fly motion under gravity. During the fly, the ball's angular velocity does not change, neither do the x- and y-components of its velocity. The z-component of the ball's velocity just before the $(i+1)$-st impact is reversed from that after the ith impact. Let $\boldsymbol{V}_k = (V_{kx}, V_{ky}, V_{kz})^T$. For $k \geq 0$, $\boldsymbol{V}_{k+1}$ and $\boldsymbol{\omega}_{k+1}$ are generated by the impact model from $\boldsymbol{V}_k$ and $\boldsymbol{\omega}_k$ if k is even; and $\boldsymbol{V}_{k+1} = (V_{kx}, V_{ky}, -V_{kz})^T$ and $\boldsymbol{\omega}_{k+1} = \boldsymbol{\omega}_k$ if k is odd.

Figure 1 in the introduction shows first five bounces initiated by a hit of the ball $\boldsymbol{V}_0 = (-1, 0, -5)$ and $\boldsymbol{\omega}_0 = (0, 2, 0)$. Table 1 lists the velocities and angular velocities of the ball right after eight consecutive bounces initiated by a hit at same velocity but a different angular velocity $\boldsymbol{\omega}_0 = (6, 6, 0)$. Observe that the z-component of the ball's velocity reduces by (roughly) half after each bounce, as determined by the coefficient of restitution $e = 0.5$. The slight discrepancies from 0.5 were due to numerical errors in integration.

Figure 13 shows the projection of the ball trajectory onto the table to be a polyline, with the first bounce at the origin (upper left corner). A dotted line connects the locations of the first and the eighth impacts on the table. Though each impact is planar, $\boldsymbol{V}_0$ does not lie in the plane spanned by $\boldsymbol{z}$ and the initial contact velocity $\boldsymbol{v}_0 = (-7, 6, -5)^T$. This explains why the overall trajectory is not straight.

8.1.3 Relationships between Pre- and Post-Impact Velocities

Suppose we keep $\boldsymbol{\omega}_0 = (0, 2, 0)^T$ while change $\boldsymbol{V}_0 = (V_{0x}, 0, -5)^T$ with V_{0x} varying in the range $[-15, 15]$. Figure 14(a) plots the post-impact velocities V_x (green) and ω_y (red), as functions of V_{0x}. Both velocity curves are anti-symmetric about the line $V_{0x} = 2$ at which the initial tangential

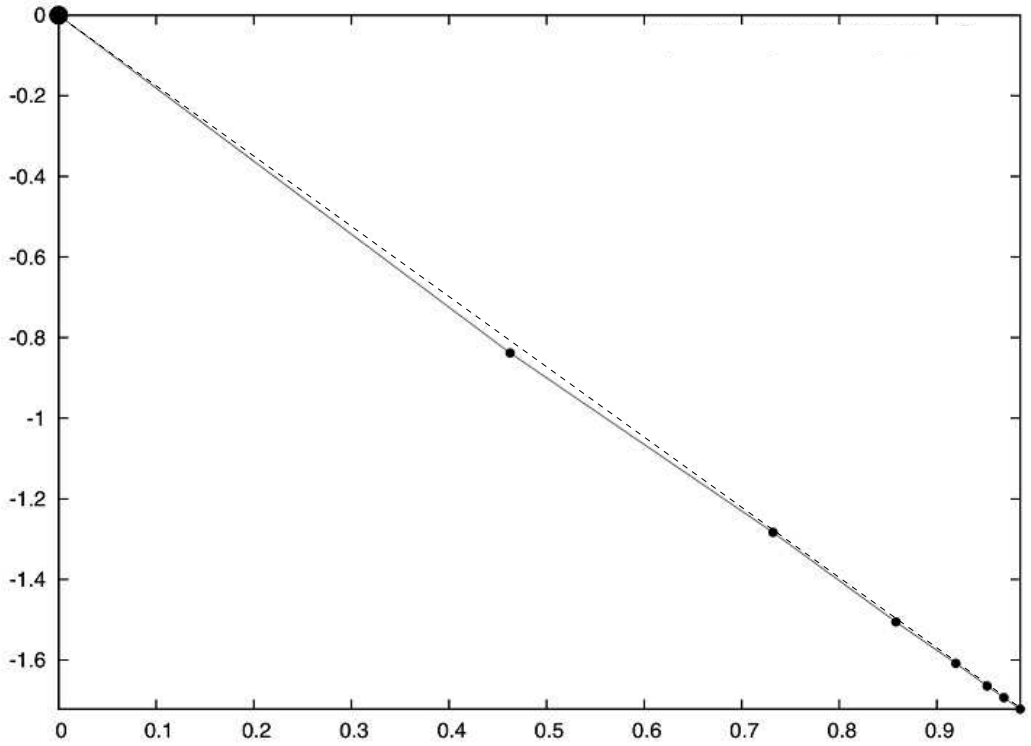

Figure 13: Trajectory of the bouncing ball determined from Table 1 as projected onto the table. Note the slight deviation from a straight trajectory (dashed).

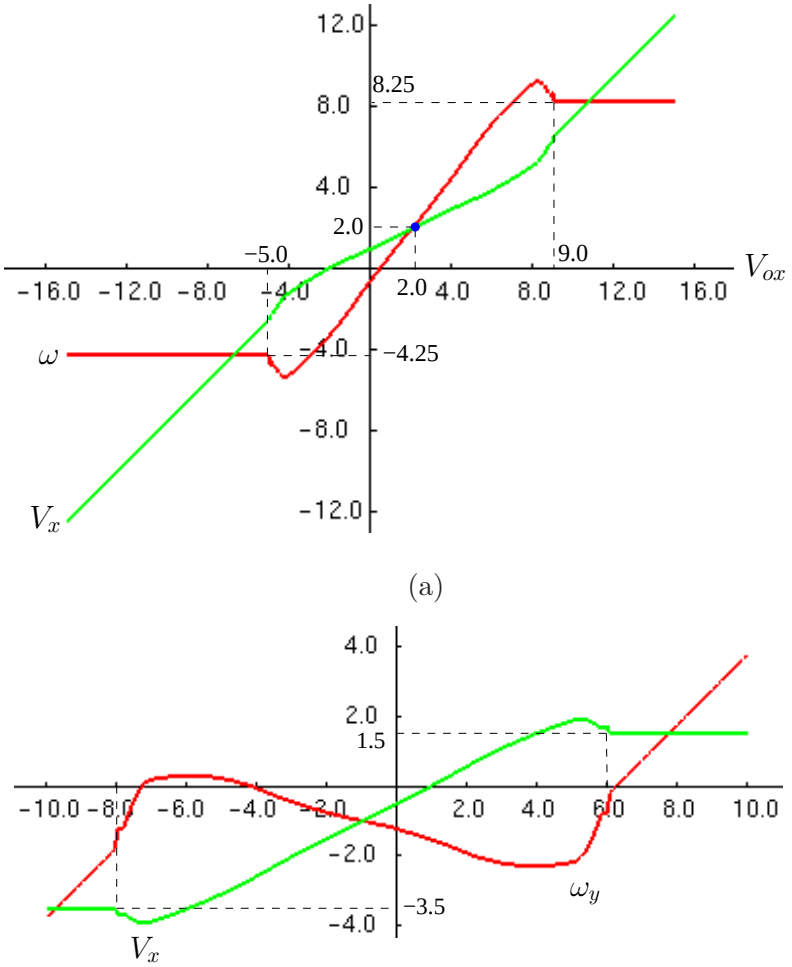

Figure 14: (a) Post-impact velocities V_x and ω_y influenced by (a) $\boldsymbol{V}_0 = (V_{0x}, 0, -5)^T$ with $V_{0x} \in [-15, 15]$ while $\boldsymbol{\omega}_0 = (0, 2, 0)^T$, and by (b) $\boldsymbol{\omega}_0 = (0, \omega_{0y}, 0)^T$ with $\omega_{0y} \in [-10, 10]$ while $\boldsymbol{V} = (-1, 0, -5)^T$.

contact velocity $v_{0x} = V_{0x} - \omega_{0y}$ is zero. The contact slips throughout the impact when $v_{0x} \leq -5$ or $v_{0x} \geq 9$ for which the tangential impulse achieves its extremum $I_x = \pm 5/2$, respectively.[12] When I_x is at an extremum, from equation (79) we easily see that V_x varies linearly with V_{0x} and $\omega_y = 2 \pm \frac{25}{4}$.

The observed extrema of $I_x = \pm 5/2$ have an absolute value sightly less than $\mu = 0.4$ times the maximum normal impulse 7.5. One reason is that under compliance dI_u/dI_n is equal to $(\alpha/\eta)\sqrt{E_u/E_n}$ according to (64) rather than μ. Another reason is that the ratio η^2 between the normal stiffness and the tangential stiffness scales up by a factor of $1/e^2$ when compression ends. Without tangential compliance, we can determine from (84) that pure sliding would happen when $V_{0x} \leq -8.5$ or $V_{0x} \geq 12.5$.

Similar patterns exist in the post-impact velocities V_x and ω_y if we fix $v_{0x} = -1$ and vary ω_y from -10 to 10. This is shown in Figure 14(b). The contact slips throughout the impact when

[12] From observation in our simulation not by a formal argument.

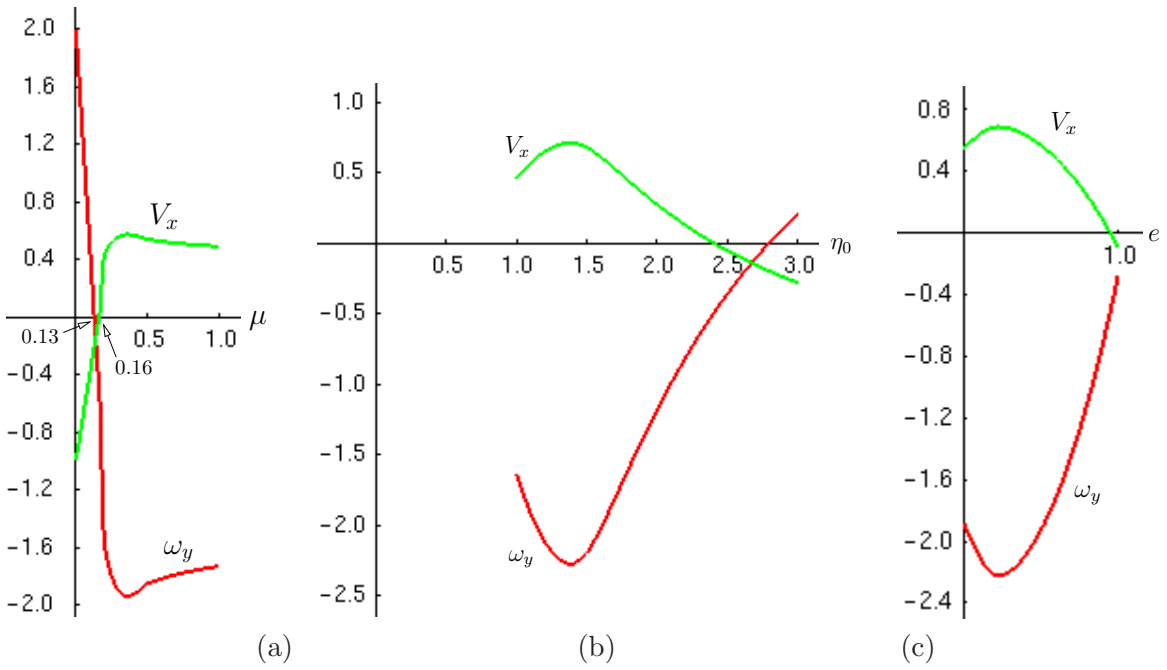

Figure 15: Post-impact velocities V_x and ω_y vary with (a) friction, (b) tangential compliance as represented by the squared root of the ratio between normal and tangential stiffnesses, and (c) coefficient of restitution.

$\omega_{0y} \leq -8.0$ or $\omega_{0y} \geq 6.0$, resulting in a constant velocity $V_x = -3.5$ or 1.5, and a w_y segment with slope 1 as determined by (79).

8.1.4 Effects of Friction, Tangential Compliance, and Coefficient of Restitution

Consider the ball's pre-impact velocities $\boldsymbol{V}_0 = (-1, 0, -5)^T$ and $\boldsymbol{\omega}_0 = (0, 2, 0)^T$. The tangential contact velocity has initial value $\boldsymbol{V}_\perp = (-3, 0, 0)^T$.

Figure 15(a) plots the post-impact velocities V_x and ω_y as the coefficient of friction varies from 0 to 1. When μ increases from 0, V_x increases monotonically while ω_y decreases monotonically. At $\mu = 0.36$, the velocities reach their extrema $V_x = 0.575906$ and $\omega = -1.93976$, respectively. As μ continues to increase, V_x decreases while ω_y increases. When friction is low ($\mu \leq 0.13$), the ball will bounce forward (i.e., to the left) with the original clockwise rotation. As μ increases from 0.13 but does not exceed 0.16, the ball will still bounce forward but reverse its rotation. As friction becomes higher ($\mu > 0.16$), the ball will bounce backward and reverse its rotation.

Figure 15(b) shows V_x and ω_y as η_0 varies from 1 to 3 with a step size of 0.05. Recall that η_0^2 is the ratio between the normal stiffness k_0 and the tangential stiffness $k_\perp$. As the value of η_0 increases, i.e., the ball-table contact becomes more compliant, the ball bounces backward. The largest V_x (i.e., backward bounce) occurs at η_0 slightly less than 1.5. Surpassing this value, more compliance yields less rebound. The ball bounces forward (i.e., along the negative x-axis) when η_0 is close to 2.4. On the other hand, more reversal of the ball rotation after the bounce occurs until η_0 has increased to a certain value, just before V_x reaches its maximum. As the contact becomes more compliant, rotation reversal decreases and eventually to zero when η_0 is around 2.6. The complex nonlinear relationships between the output velocities and tangential compliance are evidenced from

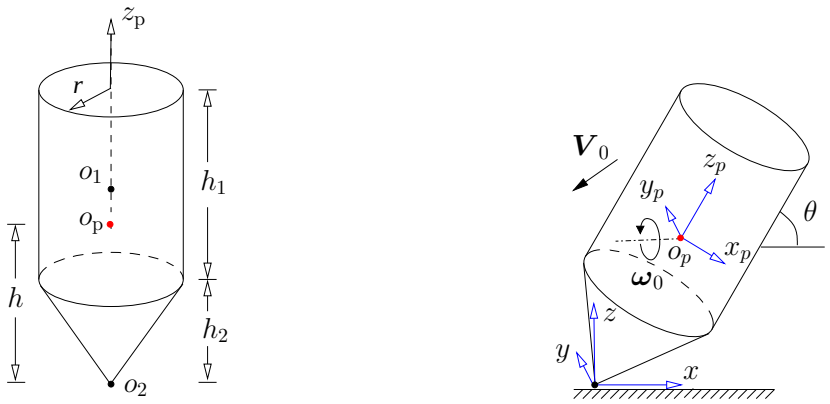

(a) (b)

Figure 16: (a) Model of a pencil; (b) striking onto a desk head down at velocities $\boldsymbol{V}_0$ and $\boldsymbol{\omega}_0$.

the occurrences of η in the denominators in the expressions (64), (68), (69), and (66) for I'_u, I'_w, E_u, E_w, $\dot{u}$, and $\dot{w}$.

Finally, we look at how the post-impact tangential velocity V_x and angular velocity ω_y vary with the coefficient of restitution e.[13] All physical constants except e have their values specified in (83). Figure 15(c) plots V_x and ω_y over the output values of 101 impact instances as e increases from 0 (plastic impact) to 1 (elastic impact) with step size 0.01. In all instances, the contact slips first, then switches to stick until compression ends. It switches back to slip before the impact ends restitution. As e increases, the magnitudes of V_x and ω_y increase until $e = 0.22$.

The plastic impact ($e = 0$) yields $\boldsymbol{V} = (0.554553, 0, 0)^T$ and $\boldsymbol{\omega} = (0, -1.88638, 0)^T$. The kinetic energy decreases from 13.4 to 0.5096 with 96.197% of energy loss. The ball slides in the positive x-direction with a rotation reversal. The elastic impact ($e = 1$) yields final velocities $\boldsymbol{V} = (-0.089745, 0, 5)^T$ and $\boldsymbol{\omega} = (0, -0.275637, 0)^T$. The loss of kinetic energy during the impact was merely 6.628%. The ball retains small portions of its previous tangential motion and rotation and bounces upward. These results suggest that as the impact becomes more elastic, the ball retains more of its original tangential motion and rotation.

8.2 Pencil-Table Collision

Let us move on to another task which many may have tried on a desk — throwing a pencil and watching it rebound. Most of the time the pencil is thrown with its rubber eraser downward, but to simplify modeling, let us consider a strike by the pencil's pointed end.

As shown in Figure 16(a), we model the pencil as a cylinder with mass m_1 and height h_1 on top of a cone with mass m_2 and height h_2. Both components have the same mass density. The cylinder's cross section and the cone's top face have the same radius r. The center of the cylinder is at o_1, while the vertex of the cone is at o_2. The pencil's center of mass $o_{\rm p}$ is located on its axis of symmetry at distance h from o_2, where $h = (6h_1^2 + 12h_1h_2 + 3h_2^2)/(12h_1 + 4h_2)$ as derived in Appendix 9. A body frame $\mathcal{B} : x_{\rm p}$-$y_{\rm p}$-$z_{\rm p}$ is placed at $o_{\rm p}$ with the $z_{\rm p}$-axis aligned with the pencil's axis of symmetry.

[13] The post-impact normal velocity is $-ev_{0n}$.

Appendix 9 also derives the moment of inertia Q of the pencil about its center of mass $o_{\rm p}$, which is a diagonal matrix with the first two principal moments as below:

$$Q_{11} = Q_{22} = \frac{m}{h_1 + h_2/3}\left(h_1\Big(\frac{3r^2 + h_1^2}{12} + l^2\Big) + \frac{h_2}{3}\left(\frac{3}{5}\Big(\frac{r^2}{4} + h_2^2\Big) + h^2\right)\right), \tag{85}$$

where $m = m_1 + m_2$ and $l = h_1/2 + h_2 - h$.

The pencil's axis always lies in some vertical plane at the moment of the strike. Let this plane be both the x-z plane of the desk frame at the contact point and the $x_{\rm p}$-$z_{\rm p}$ plane of the pencil frame $\mathcal{B}$. See Figure 16(b). Just before the hit, the pencil, tilted at an angle θ, has velocity $\boldsymbol{V}_0$ relative to the desk frame and angular velocity $\boldsymbol{\omega}_0 = (\omega_1, \omega_2, \omega_3)^T$ relative to a (fixed) frame instantaneously coinciding with the pencil frame. The orientation of the pencil frame relative to the desk frame is described by a rotation matrix R about the y-axis through $\frac{\pi}{2} - \theta$:

$$R = \begin{pmatrix} \sin\theta & 0 & \cos\theta \\ 0 & 1 & 0 \\ -\cos\theta & 0 & \sin\theta \end{pmatrix}. \tag{86}$$

The velocities are determined from the impulse $\boldsymbol{I} = (I_x, I_y, I_z)^T$ exerted on the pencil at the contact:

$$\begin{aligned} \boldsymbol{V} &= \boldsymbol{V}_0 + \frac{\boldsymbol{I}}{m}, \\ -h\hat{\boldsymbol{z}}_{\rm p} \times (R^{-1}\boldsymbol{I}) &= Q(\boldsymbol{\omega} - \boldsymbol{\omega}_0). \end{aligned}$$

The second equation above yields the angular velocity:

$$\boldsymbol{\omega} = \boldsymbol{\omega}_0 - \frac{h}{Q_{22}}(-I_y, I_x \sin\theta - I_z \cos\theta, 0)^T. \tag{87}$$

where $\boldsymbol{\omega}_0 = (\omega_1, \omega_2, \omega_3)^T$ is the pencil's angular velocity before the impact. The contact velocity during the strike is linear in $\boldsymbol{I}$:

$$\begin{aligned} \boldsymbol{v} &= \boldsymbol{V} + R(\boldsymbol{\omega} \times (0, 0, -h)^T) \\ &= \boldsymbol{V}_0 + \frac{\boldsymbol{I}}{m} + \begin{pmatrix} \sin\theta & 0 & \cos\theta \\ 0 & 1 & 0 \\ -\cos\theta & 0 & \sin\theta \end{pmatrix}\left[\begin{pmatrix} -h\omega_2 \\ h\omega_1 \\ 0 \end{pmatrix} + \frac{h^2}{Q_{22}}\begin{pmatrix} I_x \sin\theta - I_z \cos\theta \\ I_y \\ 0 \end{pmatrix}\right] \\ &= \boldsymbol{V}_0 + \frac{\boldsymbol{I}}{m} + h\begin{pmatrix} -\omega_2 \sin\theta \\ \omega_1 \\ \omega_2 \cos\theta \end{pmatrix} + \frac{h^2}{Q_{22}}\begin{pmatrix} I_x \sin^2\theta - I_z \sin\theta\cos\theta \\ I_y \\ -I_x \sin\theta\cos\theta + I_z \cos^2\theta \end{pmatrix}. \end{aligned} \tag{88}$$

Specifically, we simulate the bounce of a pencil whose mass and geometry are specified below:

$$m = 1, \qquad r = 0.5, \qquad h_1 = 3, \qquad \text{and} \qquad h_2 = 0.5. \tag{89}$$

The impact and friction parameters are chosen as

$$\mu = 0.8, \qquad \eta_0 = \sqrt{\frac{17}{14}}, \qquad \text{and} \qquad e = 0.5. \tag{90}$$

The pencil tilts at $\theta = \pi/3$, and strikes the desk with velocities

$$\boldsymbol{V}_0 = 5(-\cos\frac{\pi}{6}, 0, -\sin\frac{\pi}{6})^T \qquad \text{and} \qquad \boldsymbol{\omega}_0 = (-1, -0.5, -0.5)^T. \tag{91}$$

Figure 17 plots the 3-dimensional impulse curve and its projections onto the three impulse planes. The contact point initially slides at $\boldsymbol{v}_0 = (-3.50114, -1.91447, 0)^T$. As the normal impulse I_z increases, the contact mode switches to stick, during which compression ends. Just before restitution ends, the contact switches back to slip. The projection of the impulse curve onto the contact plane (also the I_x-I_y plane), shown in (b), indicates a continuous change in the direction of slip (or the direction of the tendency of slip when the contact sticks).

The post-impact velocities are

$$\boldsymbol{V} = (-0.467515, 0.668992, 2.86495)^T \qquad \text{and} \qquad \boldsymbol{\omega} = (0.101268, -1.59082, -0.5)^T. \tag{92}$$

The pencil bounces upward with reduced speed along the negative x-direction. It has gained a new motion along the positive y-axis. Its spin about the $x_{\rm p}$-axis has been reversed (with less magnitude) while its spin about the $y_{\rm p}$-axis has increased, all with respect to the pencil's body frame. The component of $\boldsymbol{\omega}$ along the $z_{\rm p}$ axis, i.e., the axis of symmetry, remains -0.5, due to zero torque about the axis during the impact. The total kinetic energy of the pencil has reduced from 12.5375 to 4.71613.

Figure 18 animates the pencil's motion from 0.4 second before the impact to 0.4 second after the event. Quaternions are used to update the pencil's changing orientation during the free fly motions before and after the collision. The pencil motion is sampled every 0.1 second and shown in two views for each sample time instant in (a) with the inward y-axis and (b) with the outward x-axis. Collision happens in the fifth frames in both (a) and (b). The pencil's pre-impact motion is generated via backward integration from $\boldsymbol{V}_0$ and $\boldsymbol{\omega}_0$ based on dynamics. The post-impact motion is generated via forward simulation using the velocity values (92).

9 Discussion

The introduced model for rigid body impact with tangential compliance uses a normal spring at the contact to model normal impact and two orthogonal tangential springs to model compliance. It is based on tracking the strain energies stored in these springs. The following features of the model are notable:

- Derivatives of impulses, strain energies, and velocities are all taken with respect to normal impulse.
- To detect contact slip or stick, Coulomb's friction law has been rephrased in terms of the strain energies stored by the three virtual springs at the contact point.
- The change rates of the lengths of the tangential springs with respect to time are computable based on the strain energies, so is the sliding velocity.

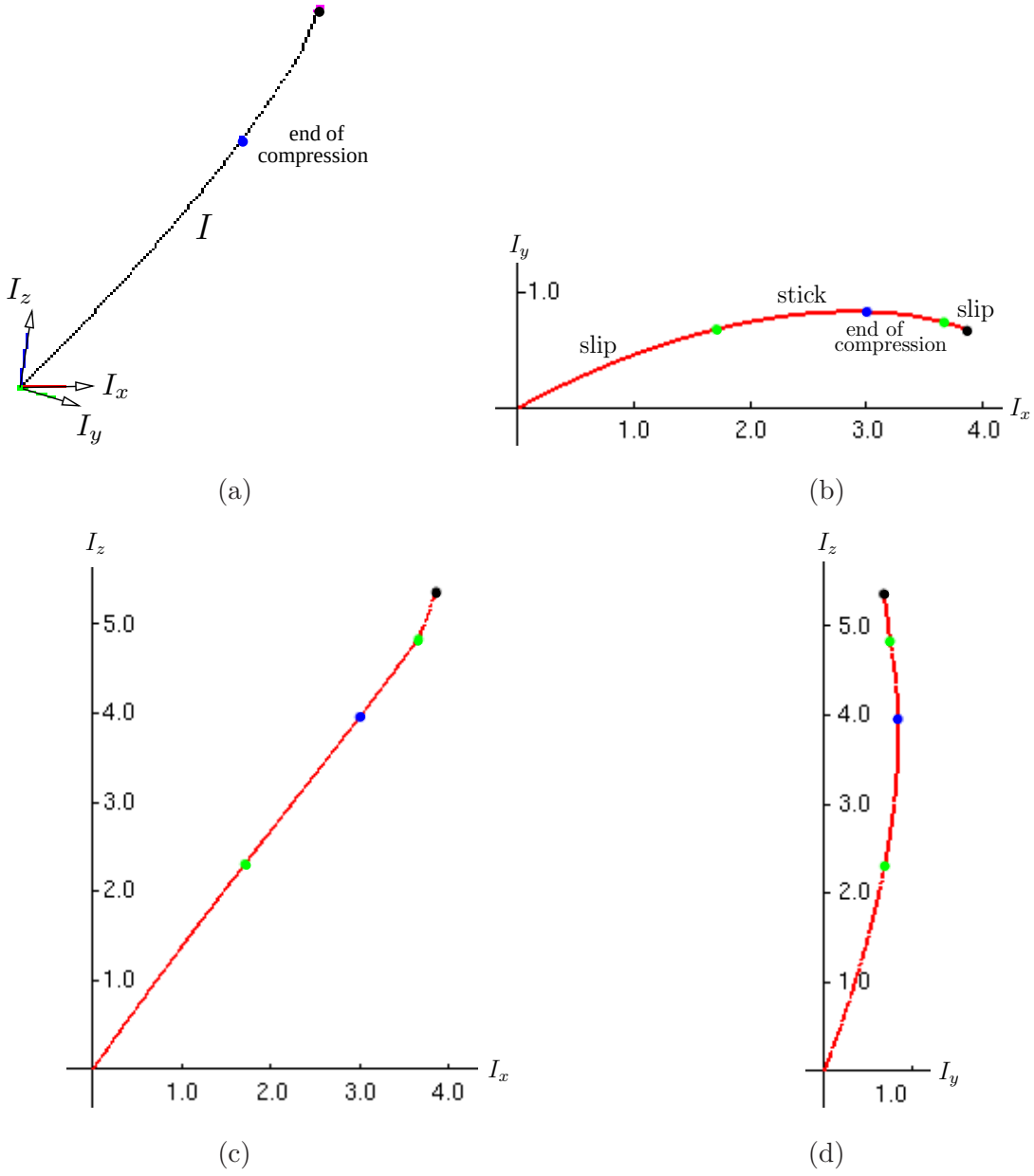

Figure 17: (a) Space impulse curve from a pencil hitting a table and its projections (b), (c), and (d) onto the three coordinate planes. During the collision, the impulse grows to $(3.86261, 0.668992, 5.36495)$. Values of the geometric and physical parameters are specified in (89)–(91).

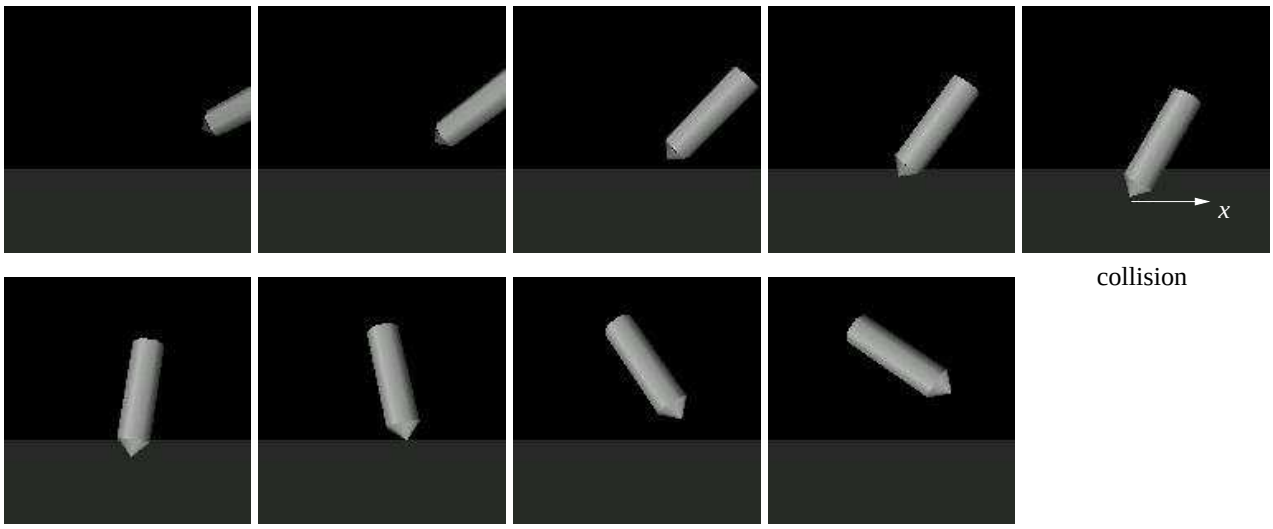

(a)

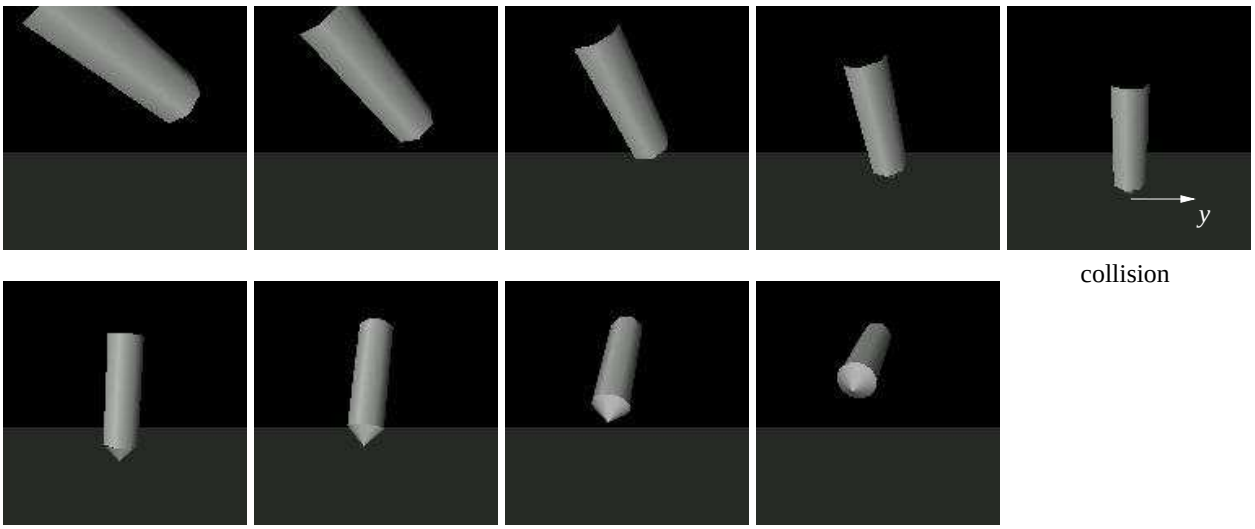

(b)

Figure 18: Pencil motion sampled at frame rate 10Hz in two different views: (a) y-axis inward and (a) x-axis outward. The z-axis is always upward. Collision happens in the fifth frame in each group.

- Special integrals G_u, G_w are updated to keep track of the length changes of the two tangential springs, scaled by a factor related to their (unknown) stiffness.

- The outcome of collision is decided by the ratio between the tangential and normal stiffnesses rather than their individual values.

These mechanisms together allow us to evaluate the tangential impulse, and eventually to simulate the whole impact system shown in Figure 8 with normal impulse (not time) as the only independent variable.

Further remarks are made about some general aspects features of the model:

- The impulse curve is generally spatial. It degenerates into a plane curve depending on the collision configuration as well as the initial contact velocity.

- The post-impact velocities scale with the pre-impact velocities.

- The impact model inputs contact velocity and normal impulse and outputs tangential impulse.

- The computed tangential impulse, combined with the accumulating normal impulse, updates the velocities of individual bodies and the contact velocity according to dynamics and contact kinematics. The updated velocity information is fed back to the model to close the loop.

The model for tangential impulse is *modular* in that it can be integrated into a multibody system with one copy for each contact, in combination with a model governing normal impulses at all contacts. A companion submission (Jia et al. 2011) investigates a model for simultaneous impacts, and integrates it with the compliant impact model. The integrated model is demonstrated over simulating a massé billiard shot, yielding a good match between the billiard trajectory reconstructed from video and one predicted by the integrated model.

The highly nonlinear nature of impulse accumulation due to contact compliance would present an obstacle for a linear complementary formulation. Our method is also more accurate since it does not use polyhedral approximation of the contact friction cone.

The presented work could pave the way for impulse-based robotic manipulation where the ability to deal with friction and tangential compliance is vital for skillful maneuvers. It also has potential impact over dynamic simulation of collisions in the field of computer graphics, where most related work has focused on collision detection. Known work on impulsed-based dynamic simulation, such as Mirtich and Canny (1995), does not model tangential compliance.

Our future work will look into measuring of relative stiffness, namely, the ratio between the normal and tangential stiffnesses. This is important for a thorough experimental validation. We plan to develop a graphical interface for simulation of sequential and simultaneous collisions among rigid bodies with friction and contact compliance. Next, we will apply the impact model to impulsive robotic manipulation. The graphical interface will be extended for simulating the executions of manipulation strategies to aid their design and implementation. A particularly interesting task would be to design a robot able to play billiards at the human level. None of the developed systems (Moore et al. 1995; Long et al. 2004; Ho et al. 2007) execute shots by exploiting the underlying impact mechanics.

Acknowledgment

This work was sponsored in part by Iowa State University. Part of the work was performed during breaks in China under self-support. The author would like to thank Matt Mason for a pointer to Stronge's work on modeling compliance in impact mechanics, and Mike Erdmann for his encouragement. Thanks also go to Rex Fernando, an ISU undergraduate, for graphical simulation of the bouncing ball and pencil based on velocity profiles generated using the impact model. An earlier version (Jia 2010) of the paper was presented at the Ninth International Workshop on Algorithmic Foundations of Robotics. The author is grateful to the anonymous workshop reviewers for their valuable and constructive feedback. He would also like to acknowledge the National Science Foundation grant IIS-0915876 that covered the expense of attending the workshop.

References

[1] Ahmed S, Lankarani HM and Pereira, MFOS (1999) Frictional impact analysis in open-loop multibody mechanical systems. *Journal of Applied Mechanics*, 121: 119–126.

[2] Anitescu M and Porta FA (1997) Formulating dynamic multi-rigid-body contact problems with friction as solvable linear complementarity problems. *Nonlinear Dynamics*, 14: 231–247.

[3] Baraff D (1993) Issues in computing contact forces for non-penetrating rigid bodies. *Algorithmica*, 8(10): 292–352.

[4] Batlle JA (1996) The sliding velocity flow of rough collisions in multibody systems. *Transactions of the ASME*, 63: 804–809.

[5] Bernoulli J (1969–1993) *Die Werk von Jakob Bernoulli*. Birkhäuser, Basel.

[6] Bhatt V and Koechling J (1994) Classifying dynamic behavior during three dimensional frictional rigid body impact. In: *Proceedings of the IEEE International Conference on Robotics and Automation*, pp. 2342–2348.

[7] Bilbao J, Campos J and Bastero C (1989) On the planar impact of an elastic body with a rough surface. *International Journal of Mechanical Engineering Education*, 17(3): 205–210.

[8] Boothroyd G and Redford AH (1968) *Mechanized Assembly: Fundamentals of Parts Feeding, Orientation, and Mechanized Assembly*. London: McGraw-Hill Inc.

[9] Brach RM (1989) Rigid body collisions. *Journal of Applied Mechanics*, 56: 133–137.

[10] Brogliato B (1999) *Nonsmooth Mechanics*. Springer, 2nd edition.

[11] Chatterjee A and Ruina A (1988) A new algebraic rigid-body collision law based on impulse space considerations. *Journal of Applied Mechanics*, 65: 939–951.

[12] Cross R (2010) Impact of a ball on a surface with tangential compliance. *American Journal of Physics*, 78(7): 716–720.

[13] Cottle R, Pang J-S and Potra FA (1996) Formulating 3D contact dynamics problems. *Mechanics of Structures and Machines*, 24(4): 405–437.

[14] Darboux G (1880) Etude géométrique sur les percussions et le choc des corps. *Bulletin des Sciences Mathématiques et Astronomiques, deuxième série*, 4: 126–160.

[15] García E and de Santos PG (2005) An improved energy stability margin for walking machines. *Robotica*, 23(1): 13–20.

[16] Glocker G (2001) On frictionless impact models in rigid-body systems. *Philosophical Transactions of the Royal Society A*, 359: 2385–2404.

[17] Glocker G and Pfeiffer F (1995) Multiple impacts with friction in rigid multibody systems. *Nonlinear Dynamics*, 7: 471–497.

[18] Han I and Gilmore BJ (1989) Impact analysis for multiple-body systems with friction and sliding contact. In D. P. Sathyadev (ed.), *Flexible Assembly Systems*, pages 99–108. ASME Design Engineering Division.

[19] Han I and Park S-U (2001) Impulsive motion planning for positioning and orienting a polygonal part. *The International Journal of Robotics Research*, 20(3): 249–262.

[20] Hien T (2010) A correction on the calculation of frictional dissipation in planar impact of rough compliant bodies by W. J. Stronge. *International Journal of Impact Engineering*, 37: 995–998.

[21] Higuchi T (1985) Application of electromagnetic impulsive force to precise positioning tools in robot systems. In: *Robotics Research: The Second International Symposium*, O. Faugeras and G. Giralt (eds.), Cambridge, MA: The MIT Press, pp. 281–285.

[22] Hirai S, Niwa M and Kawamura S (1999) Development of impulsive object sorting device with air floating. In: *Proceedings of the IEEE International Conference on Robotics and Automation*, pp. 3065–3070.

[23] Ho KHL, Martin T and Baldwin J (2007) Snooker robot player — 20 years on. In: *Proceedings of the IEEE Symposium on Computational Intelligence and Games*, pp. 1–8.

[24] Huang WH and Mason MT (2000) Mechanics, planning, and control for tapping. *The International Journal of Robotics Research*, 19(10): 883–894.

[25] Ivanov AP (1995) On multiple impact. *Journal of Applied Mathematics and Mechanics*, 59(6): 887–902.

[26] Izumi T and Kitaka Y (1993) Control of a hitting velocity and direction for a hammering robot using a flexible link. *Journal of the RSJ*, 11: 436-443 (in Japanese).

[27] Jia Y-B (2010) Energy-based motion of tangential compliance in 3-dimensional impact. In: *Algorithmic Foundations of Robotics IX*, D. Hsu et al. (eds.), Berlin Heidelberg: Springer-Verlag, pp. 267–284.

[28] Jia Y-B, Mason MT and Erdmann MA (2008) A state transition diagram for simultaneous collisions with application in billiard shooting. In: *Algorithmic Foundations of Robotics VIII*, G. S. Chirikjian et al. (eds.), Berlin Heidelberg: Springer-Verlag, pp. 135–150, 2010. Also presented at the Eighth International Workshop on Algorithmic Foundations of Robotics, Guanajuato, Mexico, 2008.

[29] Jia Y-B, Mason MT and Erdmann MA (2011) Simultaneous impacts: modeling with a state transition diagram and application to multibody systems with friction and compliance. Submitted to *The International Journal of Robotics Research*. `http://www.cs.iastate.edu/~jia/papers/IJRR11b-submit.pdf`.

[30] Johansson L (2001) A Newton method for rigid body frictional impact with multiple simultaneous impact points. *Computer Methods in Applied Mechanics and Engineering*, 191: 239–254.

[31] Johnson KL (1985) *Contact Mechanics*. Cambridge University Press.

[32] Keller JB (1986) Impact with friction. *Journal of Applied Mechanics*, 53(1): 1–4.

[33] Khatib O and Burdick J (1986) Motion and force control of robot manipulators. In: *Proceedings of the IEEE International Conference on Robotics and Automation*, pp. 1381–1386.

[34] Konno A, Myojin T, Matsumoto T, Tsujita T and Uchiyama M (2011) An impact dynamics model and sequential optimization to generate impact motions for a humanoid robot. *The International Journal of Robotics Research*, 30(13): 1596–1608.

[35] Kuipers JB (1999) *Quaternions and Rotation Sequences*. Princeton, NJ: Princeton University Press.

[36] Lankarani HM (2000) A Poisson-based formulation for frictional impact analysis of multibody mechanical systems with open or closed kinematic chains. *Journal of Mechanical Design*, 122(489-497).

[37] Liu C, Zhao Z and Brogliato B (2008) Frictionless multiple impacts in multibody systems. i. theoretical framework. *Proceedings of the Royal Society of London A*, 464: 3193–3211.

[38] Liu C, Zhao Z and Brogliato B (2009) Frictionless multiple impacts in multibody systems. ii. numerical algorithm and simulation results. *Proceedings of the Royal Society of London A*, 465: 1–23.

[39] Long F, Herland J, Tessier M-C, Naulls D, Roth A, Roth G and Greenspan M (2004) Robotic pool: an experiment in automatic potting. In: *Proceedings of the IEEE/RSJ International Conference on Intelligent Robots and Systems*, pp. 2520–2525.

[40] MacLaurin C (1742) *A Treatise on Fluxions*. Edinburgh: Ruddimans.

[41] Mason MT (1981) Compliance and force control for computer controlled manipulators. *IEEE Transactions on Systems, Man, and Cybernetics*, SMC-11(6): 418–432.

[42] Mason MT (2001) *Mechanics of Robotic Manipulation*. Cambridge, MA: The MIT Press.

[43] Maw N, Barber JR and Fawcett JN (1976) The oblique impact of elastic spheres. *Wear*, 38(1): 101–114.

[44] Mills JK and Nguyen CV (1992) Robotic manipulator collisions: modeling and simulation. *Journal of Dynamic Systems, Measurement and Control*, 114: 650–658.

[45] Mindlin RD (1949) Compliance of elastic bodies in contact. *Journal of Applied Mechanics*, 71: 259–268.

[46] Mirtich B and Canny J (1995) Impulse-based simulation of rigid bodies. In: *Proceedings of the Symposium on Interactive 3D Graphics*, Monterrey, CA, pp. 181–188.

[47] Moore AW, Hill DJ and Johnson MP (1995) An empirical investigation of brute force to choose features, smoothers and function approximators. In S. J. Hanson et al. (eds.), *Computational Learning Theory and Natural Learning*, The MIT Press, pp. 361–379.

[48] Moreau JJ (1988) Unilateral contact and dry friction in finite freedom dynamics. In J. J. Moreau and P. D. Panagiotopoulos (eds.), *Non-smooth Mechanics and Applications*, pp. 1–82. CISM Courses and Lectures, vol. 302.

[49] Partridge CB and Spong MW (1999) Control of planar rigid body sliding with impacts and friction. *The International Journal of Robotics Research* 19(4): 336-348.

[50] Raibert M (1986) *Legged Robots That Balance*. Cambridge, MA: The MIT Press.

[51] Raibert MH and Craig JJ (1981) Hybrid position/force control of manipulators. *Journal of Dynamic Systems, Measurement, and Control, Transaction of the ASME*, 102: 126–133.

[52] Routh EJ (1905) *Dynamics of a System of Rigid Bodies*. London: MacMillan and Co.

[53] Sentis L, Park J and Khatib O (2000) Compliant control of multicontact and center-of-mass behaviors in humanoid robots. *IEEE Transactions on Robotics*, 26(3): 483–501.

[54] Shamos MI (1993) *The Illustrated Encyclopedia of Billiards*. Lyons and Burford Publishers.

[55] Smith CE (1991) Predicting rebounds using rigid-body dynamics. *Transactions of the ASME*, 58: 754–758.

[56] Stewart DE and Trinkle JC (1996) An implicit time-stepping scheme for rigid body dynamics with inelastic collisions and Coulomb friction. *International Journal for Numerical Methods in Engineering*, 39: 2673–2691.

[57] Stronge WJ (1990) Rigid body collisions with friction. *Proceedings of the Royal Society of London A*, 431: 168–181.

[58] Stronge WJ (1994) Planar impact of rough compliant bodies. *International Journal of Impact Engineering*, 15(4): 435–450.

[59] Stronge WJ (2000) *Impact Mechanics*. Cambridge University Press.

[60] Tagawa K, Hirota K and Hirose M (2010) Manipulation of dynamically deformable object using impulse-based approach. In M. H. Zadeh (ed.), *Advances in Haptics*, pp. 16–33.

[61] Tang P and Xiao J (2008) Automatic generation of high-level contact state space between 3D curved objects. *The International Journal of Robotics Research*, 27(7): 832–854.

[62] Van Damme M, Beyl P, Vanderborght B, Van Ham R, Vanderniepen I, Matthys A, Cherelle P and Lefeber D (2010) The role of compliance in robot safety. In: *Proceedings of the Seventh IARP Workshop on Technical Challenges for Dependable Robots in Human Environments*, pp. 65–71.

[63] Volpe R and Khosla P (1993) A theoretical and experimental investigation of impact control for manipulators. *The International Journal of Robotics Research*, 12: 351-365.

[64] Walker ID (1994) Impact configurations and measures for kinematically redundant and multiple armed robot system. *IEEE Transactions on Robotics and Automation*, 10: 670-683.

[65] Wang Y-T, Kumar V and A Jacob (1992) Dynamics of rigid bodies undergoing multiple frictional contacts. In: *Proceedings of the IEEE International Conference on Robotics and Automation*, pp. 2764–2769.

[66] Wang Y and Mason MT (1992) Two-dimensional rigid-body collisions with friction. *Journal of Applied Mechanics*, 59: 635–642.

[67] Whitney DE (1982) Quasi-static assembly of compliantly supported rigid parts. *Journal of Dynamic Systems, Measurement, and Control, Transaction of the ASME*, 104: 65–76.

[68] Yoshida K and Nenchev DN (1995) Space robot impact analysis and satellite-base impulse minimization using reaction nullspace. In: *Proceedings of the IEEE International Conference on Robotics and Automation*. pp. 1271–1277.

[69] Zhao Z, Liu C and Brogliato B (2009) Planar dynamics of a rigid body system with frictional impacts. ii. qualitative analysis and numerical simulations. *Proceedings of the Royal Society A: Mathematical, Physical & Engineering Sciences*, 465: 2267–2292.

[70] Zheng YF and Hemami H (1985) Mathematical modeling of a robot collision with its environment. *Journal of Robotic Systems*, 2: 289–307.

Appendix A: Initial Energy Ratios

This appendix derives the initial values of the ratios of the energies E_u and E_w stored by the two tangential springs to the energy E_n stored by the normal spring. Because $E_u = E_w = E_n = 0$, the ratios need to be determined via taking their limits as the normal impulse $I_n \to 0$. We make use of the following facts:

$$\begin{aligned} \frac{dE_u}{dI_u} &= \frac{\dot{E}_u}{\dot{I}_u} = \frac{k_\perp u \dot{u}}{-k_\perp u} = -\dot{u}, \\ \frac{dE_w}{dI_w} &= -\dot{w}. \end{aligned}$$

When the contact initially sticks, $\dot{u} = v_{0u}$ and $\dot{w} = v_{0w}$ from (38) and (39). We have

$$\begin{aligned} \lim_{I_n \to 0} \frac{E_u}{E_n} &= \lim_{I_n \to 0} \frac{E'_u}{E'_n} && \text{by L'Hospital's rule} \\ &= \lim_{I_n \to 0} \frac{(dE_u/dI_u) \cdot I'_u}{-v_n} && \text{by (18)} \\ &= \lim_{I_n \to 0} \frac{-\dot{u} \cdot I'_u}{-v_n} \\ &= \frac{v_{0u}}{v_{0n}\eta_0} \lim_{I_n \to 0} \sqrt{\frac{E_u}{E_n}} && \text{by (23) with } \alpha = -1. \end{aligned}$$

Solve the equation:

$$\lim_{I_n \to 0} \frac{E_u}{E_n} = \left(\frac{v_{0u}}{v_{0n}\eta_0} \right)^2. \tag{93}$$

The other solution zero is discarded because the initial tangential force exerted on the u-spring is a non-zero fraction of that exerted on the n-spring, since the particle to which both springs are attached does not move. Similarly, we obtain the initial ratio

$$\lim_{I_n \to 0} \frac{E_w}{E_n} = \left(\frac{v_{0w}}{v_{0n}\eta_0} \right)^2 \;=\; 0, \tag{94}$$

since $v_{0w} = 0$.

When the contact initially slips, the sliding velocity $\boldsymbol{v}_s$ is in the direction of $-\hat{\boldsymbol{u}}$. There is no motion in the orthogonal direction $\hat{\boldsymbol{w}}$. Hence $\dot{w} = 0$. We apply L'Hospital's rule:

$$\begin{aligned} \lim_{I_n \to 0} \frac{E_w}{E_u} &= \lim_{I_n \to 0} \frac{\dot{E}_w}{\dot{E}_u} = \lim_{I_n \to 0} \frac{w\dot{w}}{u\dot{u}} \\ &= \lim_{I_n \to 0} \frac{\dot{w}^2 + w\ddot{w}}{(\dot{u}^2 + u\ddot{u})} = \frac{\dot{w}(0)^2}{\dot{u}(0)^2} \\ &= 0. \end{aligned}$$

The above, combined with (46), implies that

$$\lim_{I_n \to 0} \frac{E_u}{E_n} = \mu^2\eta_0^2 \qquad \text{and} \qquad \lim_{I_n \to 0} \frac{E_w}{E_n} = 0. \tag{95}$$

Take the limits of $\dot{u}$ and $\dot{w}$ in (48) and (49) as $I_n \to 0$ (setting $\alpha = -1$ due to compression): $\dot{u}(0) = \mu\eta_0^2 v_{0n}$ and $\dot{w}(0) = 0$.

Appendix B: Initial Changes in Length of the Tangential Springs

The initial contact mode is decided from $\boldsymbol{v}_0 = v_{0u}\hat{\boldsymbol{u}} + v_{0w}\hat{\boldsymbol{w}} + v_{0n}\hat{\boldsymbol{n}}$ according to Proposition 1. We here look at how $G_u = \sqrt{2k_0}u$ and $G_w = \sqrt{2k_0}w$ vary as I_n increases from 0. Given (65) we have from the Taylor series of E_n about $I_n = 0$:

$$E_n = -v_{0n}I_n + O(I_n^2). \tag{96}$$

The Taylor series of $1/\sqrt{E_n}$, this time about $-v_{0n}I_n$, is

$$\begin{aligned} \frac{1}{\sqrt{E_n}} &= \frac{1}{\sqrt{-v_{0n}I_n + O(I_n^2)}} \\ &= \frac{1}{\sqrt{-v_{0n}I_n}} + \frac{v_{0n}}{2(-v_{0n}I_n)^{3/2}} \cdot O(I_n^2) \\ &= \frac{1}{\sqrt{-v_{0n}I_n}} + O(\sqrt{I_n}). \end{aligned} \tag{97}$$

Meanwhile, using (61) and (62) we apply the Taylor expansion to the impulse about $I_n = 0$:

$$\boldsymbol{I} = (I_u'(0)\hat{\boldsymbol{u}} + \hat{\boldsymbol{n}})I_n + O(I_n^2). \tag{98}$$

Substitute (98) into (63):

$$\boldsymbol{v} = \boldsymbol{v}_0 + O(I_n),$$

and in particular,

$$v_u = v_{0u} + O(I_n). \tag{99}$$

Suppose the contact sticks initially. From (38) and (39), $\dot{u} = v_{0u}$ and $\dot{w} = v_{0w}$ at the start. We substitute (97) and (99) into the integrals (27) and (28):

$$\begin{aligned} G_u(I_n) &= \int_0^{I_n} \frac{v_u}{\sqrt{E_n}}\, dI_n \\ &= \int_0^{I_n} (v_{0u} + O(I_n)) \cdot \left(\frac{1}{\sqrt{-v_{0n} I_n}} + O(\sqrt{I_n}) \right) dI_n \\ &= \frac{2v_{0u}}{\sqrt{-v_{0n}}} \sqrt{I_n} + O(I_n^{3/2}), \end{aligned} \tag{100}$$

$$\begin{aligned} G_w(I_n) &= \frac{2v_{0w}}{\sqrt{-v_{0n}}} \sqrt{I_n} + O(I_n^{3/2}) \\ &= O(I_n^{3/2}). \end{aligned} \tag{101}$$

The last equation above follows from $v_{0w} = 0$ since $\hat{\boldsymbol{w}}$ is chosen to be orthogonal to $\boldsymbol{v}_{0\perp}$.

Consider initial slip at the contact. The limit of the energy ratio E_u/E_n in (95) implies that

$$\frac{E_u}{E_w} = \mu^2 \eta_0^2 + o(1).$$

In the above equation, we substitute (30) for E_u and (96) for E_n. This yields

$$G_u^2 = 4\mu^2 \eta_0^4 (-v_{0n}) I_n + o(I_n).$$

Take the negative square root of the right hand side above (since at the start the u-spring is compressed), and apply the Taylor expansion about $\sqrt{-v_{0n} I_n}$. We obtain

$$G_u(I_n) = 2\mu^2 \eta_0^2 \sqrt{-v_{0n} I_n} + o(I_n). \tag{102}$$

That $\dot{w}(0) = 0$ follows from (32), and $\hat{\boldsymbol{u}} \cdot \boldsymbol{v}_{0\perp} < 0$ due to slip. There exists a small enough period after the start such that either $v_w < \dot{w} < 0$ or $0 < \dot{w} < v_w$. This, combined with the definition (28) of G_w, implies that

$$\left| \int_0^{I_n} \frac{v_w}{\sqrt{E_n}}\, dI_n \right| > |G_w|.$$

The above inequality, together with (101), implies that

$$G_w(I_n) = O(I_n^{3/2}). \tag{103}$$

Appendix C: Pencil's Angular Inertia

This section derives the moment of inertia of the pencil in Figure 16. First, we calculate its center of mass o_{p}, which is on the axis of symmetry and at distance h above the cone's vertex o_2. The

conic section has its center at distance $\frac{3}{4}h_2$ above its vertex. Since the pencil has uniform mass density, its cylindrical and conic sections have masses proportional to their volumes. Hence

$$\begin{aligned} h &= \frac{\pi r^2 h_1}{\pi r^2 h_1 + \frac{1}{3}\pi r^2 h_2} \cdot \left(h_2 + \frac{h_1}{2}\right) + \frac{\frac{1}{3}\pi r^2 h_2}{\pi r^2 h_1 + \frac{1}{3}\pi r^2 h_2} \cdot \frac{3}{4} h_2 \\ &= \frac{h_1}{h_1 + \frac{1}{3}h_2}\left(h_2 + \frac{h_1}{2}\right) + \frac{\frac{1}{3}h_2}{h_1 + \frac{1}{3}h_2} \cdot \frac{3}{4} h_2 \\ &= \frac{6h_1^2 + 12h_1h_2 + 3h_2^2}{12h_1 + 4h_2}. \end{aligned}$$

The inertia matrices Q_1 and Q_2 of the cylinder and the cone in their canonical frames at o_1 and o_2 (cf. Figure 16), respectively, are known to be

$$\begin{aligned} Q_1 &= \begin{pmatrix} \frac{1}{4}r^2 + \frac{1}{12}h_1^2 & 0 & 0 \\ 0 & \frac{1}{4}r^2 + \frac{1}{12}h_1^2 & 0 \\ 0 & 0 & r^2 \end{pmatrix}, \\ Q_2 &= \begin{pmatrix} \frac{3}{20}r^2 + \frac{3}{5}h_2^2 & 0 & 0 \\ 0 & \frac{3}{20}r^2 + \frac{3}{5}h_2^2 & 0 \\ 0 & 0 & \frac{3}{10}r^2 \end{pmatrix}. \end{aligned}$$

Suppose an object with mass m and angular inertia Q undergoes a translation of $\boldsymbol{r}$. Then its angular inertia with respect to the frame coinciding with its body frame before the translation is $Q + m(\boldsymbol{r} \cdot \boldsymbol{r})I_3 - m\boldsymbol{r}\boldsymbol{r}^T$, where I_3 is the 3×3 identity matrix. The points o_1 and o_2 are translated by $(0, 0, l)$ and $(0, 0, -h)$ from the pencil's center of mass, respectively, where $l = \frac{h_1}{2} + h_2 - h$. Therefore, its moment of inertia is

$$Q = Q_1 + m_1 l^2 I_3 - m_1 \operatorname{diag}(0, 0, l^2) + Q_2 + m_2(-h)^2 I_3 - m_2 \operatorname{diag}(0, 0, h^2). \tag{104}$$

We can easily verify the first two diagonal elements of Q given in (85).